minerals

MDPI

Article

Magmatic Redox Evolution and Porphyry–Skarn Transition in Multiphase Cu-Mo-W-Au Systems of the Eocene Tavşanlı Belt, NW Türkiye

Hüseyin Kocatürk [1,2,*], Mustafa Kumral [1], Hüseyin Sendir [3], Mustafa Kaya [1], Robert A. Creaser [2] and Amr Abdelnasser [1,4]

[1] Department of Geological Engineering, Faculty of Mines, Istanbul Technical University, Istanbul 34469, Türkiye; kumral@itu.edu.tr (M.K.); kayamusta@itu.edu.tr (M.K.); amrkhalil@itu.edu.tr (A.A.)
[2] Department of Earth and Atmospheric Sciences, Faculty of Science, University of Alberta, Edmonton, AB T6G 2E3, Canada; rcreaser@ualberta.ca
[3] Department of Geological Engineering, Faculty of Engineering and Architecture, Eskisehir Osmangazi University, Eskişehir 26040, Türkiye; hsendir@ogu.edu.tr
[4] Department of Geology, Faculty of Science, Benha University, Benha 13511, Egypt; amr.khalil@fsc.bu.edu.eg
* Correspondence: kocaturkhu@itu.edu.tr

Abstract

This study explores the magmatic and hydrothermal evolution of porphyry–skarn–transitional Cu-Mo-W-Au systems within the Nilüfer Mineralization Complex (NMC), located in the westernmost segment of the Eocene Tavşanlı Metallogenic Belt, NW Türkiye. Through integration of field data, whole-rock geochemistry, Re–Os molybdenite dating, and amphibole–biotite mineral chemistry, the petrogenetic controls on mineralization across four spatially associated mineralized regions (Kirazgedik, Güneybudaklar, Kozbudaklar, and Delice) were examined. The earliest and thermally most distinct phase is represented by the Kirazgedik porphyry system, characterized by high temperature (~930 °C), oxidized quartz monzodioritic intrusions emplaced at ~2.7 kbar. Rising fO_2 and volatile enrichment during magma ascent facilitated structurally focused Cu-Mo mineralization. At Güneybudaklar, Re–Os geochronology yields an age of ~49.9 Ma, linking Mo- and W-rich mineralization to a transitional porphyry–skarn environment developed under moderately oxidized (ΔFMQ + 1.8 to +0.5) and hydrous (up to 7 wt.% H_2O) magmatic conditions. Kozbudaklar represents a more reduced, volatile-poor skarn system, leading to Mo-enriched scheelite mineralization typical of late-stage W-skarns. The Delice system, developed at the contact of felsic cupolas and carbonates, records the broadest range of redox and fluid compositions. Mixed oxidized–reduced fluid signatures and intense fluid–rock interaction reflect complex, multistage fluid evolution involving both magmatic and external inputs. Geochemical and mineralogical trends—from increasing silica and Rb to decreasing Sr and V—trace a systematic evolution from mantle-derived to felsic, volatile-rich magmas. Structurally, mineralization is controlled by oblique fault zones that localize magma emplacement and hydrothermal flow. These findings support a unified genetic model in which porphyry and skarn mineralization styles evolved continuously from multiphase magmatic systems during syn-to-post-subduction processes, offering implications for exploration models in the Western Tethyan domain.

Keywords: porphyry–skarn systems; Cu-Mo-W-Au mineralization; magmatic redox evolution; Re–Os geochronology; amphibole–mica chemistry; post-subduction magmatism

Academic Editors: Yiwei Peng, Chao Yang and Gangyang Zhang

Received: 25 June 2025
Revised: 24 July 2025
Accepted: 25 July 2025
Published: 28 July 2025

Citation: Kocatürk, H.; Kumral, M.; Sendir, H.; Kaya, M.; Creaser, R.A.; Abdelnasser, A. Magmatic Redox Evolution and Porphyry–Skarn Transition in Multiphase Cu-Mo-W-Au Systems of the Eocene Tavşanlı Belt, NW Türkiye. *Minerals* **2025**, *15*, 792. https://doi.org/10.3390/min15080792

1. Introduction

Porphyry-related mineral systems are globally significant sources of critical metals such as copper, molybdenum, and, increasingly, gold. These deposits typically form within tectonically active orogenic belts and result from the interplay of magmatic and hydrothermal processes. A characteristic feature is a metal-enriched intrusive body that acts as the core of the system, surrounded by extensive zones of hydrothermal alteration and associated mineralization [1–6]. The evolution of these systems is strongly influenced by the behavior of magmatic fluids, which can exsolve from crystallizing magmas and interact with the surrounding host rocks. This process often leads to overlapping mineralization styles, including porphyry, skarn, greisen, and epithermal types—particularly in structurally complex settings or where there are strong lithological contrasts [7,8]. While tungsten enrichment is generally uncommon within central porphyry systems, it is frequently associated with peripheral skarn and vein-type systems. These tungsten-bearing systems typically form when metal-rich, reduced magmatic fluids interact with carbonate-rich host rocks, promoting tungsten deposition [7].

The Eocene Tavşanlı Porphyry Belt in northwest Türkiye, part of the Western Tethyan metallogenic domain, provides an ideal setting to investigate such hybrid mineral systems. This belt exemplifies the spatial and genetic relationships between porphyry and peripheral mineralization styles in a tectonically and magmatically complex setting [9] (Figure 1). Its eastern part hosts Cu-Mo porphyry deposits, including Muratdere and Kirazgedik, along with associated Cu-bearing skarns such as Gelemiç [10–12]. Conversely, the western segment is characterized predominantly by W-rich skarn systems, notably Kozbudaklar mineralization, which also exhibit Mo enrichment [13]. Within this western domain lies the Nilüfer Mineralization Complex (NMC), encompassing several centers such as Kozbudaklar, Güneybudaklar, and Delice. The NMC represents a hybrid mineral system having Cu, Mo, Au, and W, with mineralization styles comprising porphyry, skarn, and hydrothermal vein assemblages. This complex preserves a well-constrained temporal and spatial zoning of mineralization, serving as a representative example of hybrid magmatic-hydrothermal systems within the western portion of the Tavşanlı belt.

Previous studies in the Tavşanlı Zone of northwest Türkiye have primarily concentrated on isolated mineral deposits within the Eocene magmatic arc, notably the Kozbudaklar W-Mo skarn and the Kirazgedik Cu-Mo ± Au porphyry system. The Kozbudaklar skarn has been interpreted as a product of contact metasomatism between the Topuk Pluton and the Triassic İnönü Marble [13], while Kirazgedik has been linked to the South Tepeldağ Pluton and framed within a broader tectonomagmatic context of slab rollback during the waning stages of Neo-Tethyan subduction [12,14]. Although these studies provided foundational deposit-level insights, they did not explore the potential genetic and temporal relationships among the broader set of mineralized centers within the Nilüfer Mineralization Complex (NMC). As a result, the combination of porphyry, skarn, and vein-style mineralization across this area, and their integration into a coherent geodynamic and metallogenic framework, remained largely unresolved.

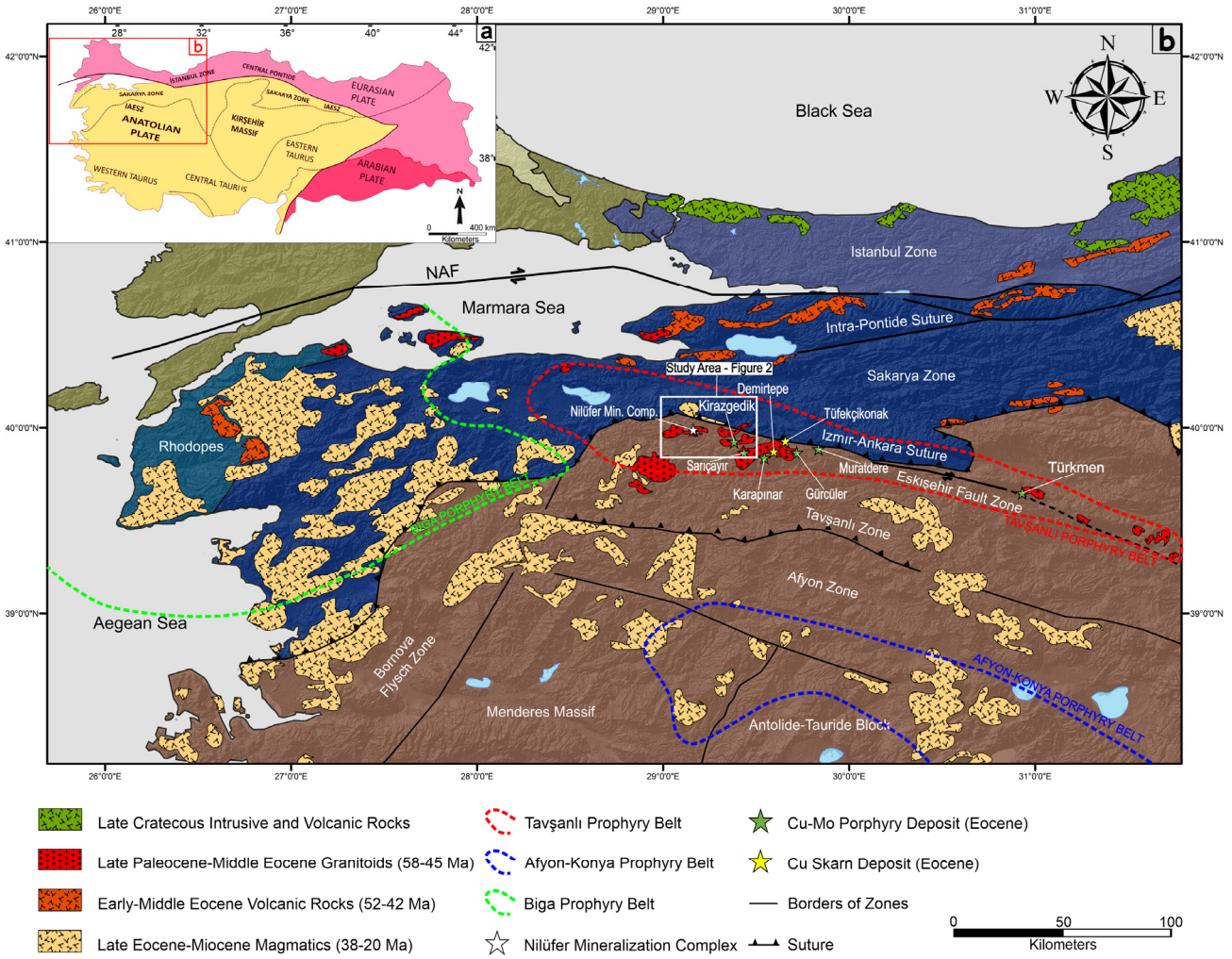

Figure 1. (**a**) Tectonic map of Turkey with major suture zones [15]; IAES: Izmir-Ankara-Erzincan suture, ITS: Inner Tauride suture. (**b**) Simplified geological map of Western Anatolia illustrating the major Eocene to Miocene porphyry belts and key tectonic features. NAF: North Anatolian Fault. Adapted from Kuşcu, et al. [16].

This study aims to evaluate whether the Nilüfer Mineralization Complex (NMC) represents a spatially zoned and evolutionarily continuous magmatic-hydrothermal system, rather than a collection of geologically isolated mineral deposits. We propose a comprehensive model of an integrated porphyry-skarn mineral system that includes four key sectors: Kirazgedik, Kozbudaklar, Güneybudaklar, and Delice (Figure 2). In this model, the mineralization associated with the Topuk Pluton, including the W-Mo skarns and related hydrothermal features, is hypothesized to be temporally and genetically linked to the Kirazgedik Cu-Mo porphyry system located to the east and hosted by the adjacent South Tepeldağ Pluton (Figure 2). To evaluate this hypothesis, a multidisciplinary methodological framework is applied. Field observations are combined with high-precision Re-Os dating of molybdenite. This is supported by electron microprobe analyses of amphibole and mica, which provide estimates of temperature, pressure, oxidation state, and volatile content (such as Cl and F), using established calibrations [17–19]. Whole-rock geochemical data and rare earth element patterns are used to evaluate the genesis and compositional evolution of all related intrusives associated with early porphyry to late-stage skarn systems [20–22].

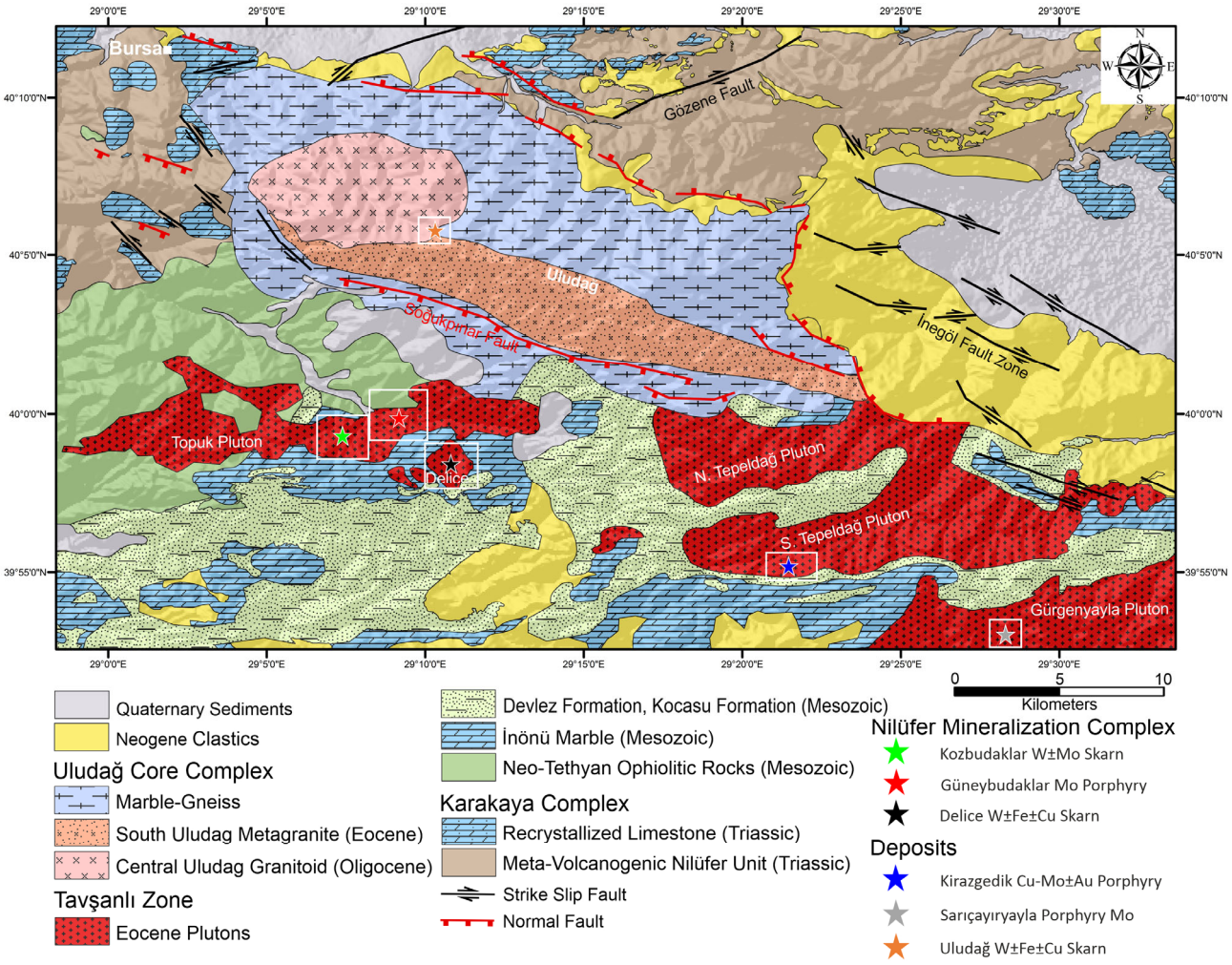

Figure 2. Schematic map of the Nilüfer Hybrid Mineralization Complex (NHMC), showing major intrusive bodies and the spatial distribution of porphyry, skarn, and vein-type mineralization styles. Modified after Kocatürk [9] and Kocatürk, et al. [14].

Consequently, this study investigates whether porphyry mineralizations of the Western Tavşanlı Metallogenic Belt and different skarn mineralizations listed under the Nilüfer Mineralization Complex represent isolated deposits or a spatially zoned and evolutionarily continuous magmatic-hydrothermal system. The presence of geochemical data, the alignment of mineralization with fault networks, and the temporal sequence among distinct deposit types indicate a response to syn- to post-subduction slab behavior, which influenced magma emplacement and ore fluid migration. As such, the study introduces a new exploration model for porphyry-skarn transitions in post-subduction settings, with broader implications for metallogenic interpretations in the Western Tethyan domain and similar orogenic belts. By integrating geochronological, petrological, and geochemical evidence, this work advances the understanding of how multi-style mineralization can evolve from a single, tectono-magmatically driven system.

2. Geological Framework

The Tavşanlı Zone (TZ), situated directly south of the İzmir-Ankara Suture Zone (IASZ), forms the northernmost margin of the Anatolide-Tauride Block and hosts the Tavşanlı Metallogenic Belt within the Bursa district (Figure 1). The zone preserves a complex tectonostratigraphic succession that records prolonged subduction-accretion processes and forms the crystalline basement upon which Eocene magmatism and associated ore-

forming events are superimposed. The pre-Cenozoic basement of the TZ is composed of three primary lithostratigraphic packages. The lowermost unit is the Orhaneli Group, a high-pressure, low-temperature (HP-LT) metamorphic complex comprising quartz-rich greyschists (Kocasu Formation), massive marbles (İnönü Marble), and heterogeneous assemblages of metabasite, phyllite, and chert (Devlez Formation). These rocks exhibit mineral assemblages of glaucophane, lawsonite, phengite, and chlorite, which are characteristic of blueschist-facies metamorphism formed under subduction-related conditions [23,24].

Overlying this metamorphic basement is a Late Cretaceous accretionary complex, consisting of a serpentinite-matrix mélange that encloses blocks of basalt, radiolarian chert, pelagic limestone, and serpentinized ultramafic rocks—interpreted as fragments of the Neotethyan oceanic crust [14,25,26]. The uppermost stratigraphic component consists of an ophiolitic sequence, primarily composed of serpentinized harzburgite, dunite, and layered gabbroic cumulates, locally intruded by plagiogranites. These ophiolites display geochemical features consistent with a supra-subduction zone (SSZ) forearc origin and are interpreted as products of Late Cretaceous obduction processes, emplaced onto the passive margin of the Anatolide–Tauride Block [27,28].

The Eocene plutonism within the TZ is represented by several multiphase intrusions, notably the Topuk, Tepeldağ, and Gürgenyayla plutons, which are emplaced into this pre-Cenozoic basement (Figure 2). These intrusions differ in petrography, mineralogy, and emplacement age, as constrained by detailed field observations and U-Pb zircon geochronology [14,29]. The Gürgenyayla Pluton, situated in the eastern part of the study area (Figure 2), consists mainly of coarse-grained, equigranular granodiorite to monzogranite, with local syenitic facies and textural evidence of magma mingling, such as mafic microgranular enclaves. Its mineral assemblage includes plagioclase, quartz, K-feldspar, hornblende, and biotite, with zircon U-Pb crystallization ages indicating emplacement at approximately 51 Ma (51.02 $\pm$ 0.52 and 51.5 $\pm$ 0.1 Ma) [12,29] into structurally elevated basement blocks during a phase of post-subduction extension.

The Tepeldağ Pluton comprises two distinct intrusive phases (Figure 2). The South Tepeldağ phase is dominated by quartz monzodioritic to quartz monzonitic rocks that are rich in hornblende and biotite, displaying hypidiomorphic granular textures, and has been dated at 54.56 $\pm$ 0.21 Ma [14]. This phase is spatially associated with the Kirazgedik porphyry Cu-Mo system, suggesting a potential genetic relationship. The North Tepeldağ phase is more felsic, comprising quartz diorite to granodiorite with porphyritic textures, as an emplacement age of approximately 45.41 $\pm$ 0.34 Ma [29].

The Topuk Pluton, located in the central part of the study area (Figure 2), is a composite intrusion comprising mainly a granodioritic body and an evolved felsic cupola known as the Delice stock (Figure 2). The main phase consists of granodiorite, quartz diorite, quartz monzodiorite, and quartz monzonite, with porphyritic to hypidiomorphic textures. The Delice cupola includes tonalite, granodiorite, and alkali feldspar granite with both granular and porphyritic textures [14]. The primary mineral assemblages include plagioclase, quartz, K-feldspar, hornblende, and biotite, with muscovite present in more evolved phases. Zircon U–Pb dating constrains the crystallization ages of the main intrusive phases of the Topuk Pluton to 48.71 $\pm$ 0.44, while the Delice stock yields slightly younger ages, ranging from 47.3 $\pm$ 0.2 Ma to 45.9 $\pm$ 0.3 Ma [9,14,29].

Peripheral intrusive facies of the Topuk Pluton correspond spatially with the ore mineralization zones of the Nilüfer Mineralization Complex (NMC). The Kozbudaklar region hosts granodioritic rocks associated with W-Mo skarn mineralization. The Güneybudaklar region is characterized by quartz monzonitic and quartz dioritic apophyses exhibiting geochemical signatures consistent with late-stage magmatic evolution and metal enrichment.

The Delice region, marked by a felsic stock, corresponds to the structural cupola of the pluton and is associated with W-Fe-Cu skarn bodies (Figure 2).

Collectively, these Eocene intrusive bodies delineate a tectono-magmatic corridor within the Tavşanlı Zone (TZ) that reflects episodic emplacement and progressive geochemical differentiation. Despite the Topuk Pluton displaying structural and mineralogical continuity with the surrounding intrusions, field evidence—such as the presence of brittle faulting and polymictic hydrothermal breccias—suggests that the NMC developed under a distinct tectonic regime. This regime was likely influenced by a deep-seated oblique fault system, which controlled magma ascent, hydrothermal fluid migration, and the localization of mineralization. A detailed summary of petrographic characteristics, textures, and geochronological data for these plutonic units in the study area is presented in Table 1, after Altunkaynak et al. [29], Kocatürk [9], and Kocatürk et al. [14].

Table 1. Petrographic Summary of Eocene Plutons of Bursa District in the Tavşanlı Zone, after Altunkaynak, et al. [29], Kocatürk [9], and Kocatürk, et al. [14].

Pluton	Sub-Unit	Rock Type	Textures	Main Minerals	References
Topuk	Main Body	Grd, Qz-Di, Qz-Mzd, Qz-Mzn	Porphyritic, hypidiomorphic	Grd: Pl, Qz, Kfs, Hb, Bt; Qz-Mzd: Pl, Qz, Kfs, Hb, Bt; Qz-Mzn: Pl, Qz, Kfs, Bt, Hb	Altunkaynak, et al. [29]; Kocatürk, et al. [14]
	Delice	Ton, Grd, Afs-Gr	Granular, porphyritic	Ton: Pl ↑, Qz ↑, Hb, Bt, Kfs ↓; Grd: Pl, Qz, Kfs, Hb, Bt; Afs-Gr: Kfs ↑, Qz, Pl ↓, Bt, Ms	Kocatürk, et al. [14]
Tepeldağ	South Tepeldağ	Qz-Mzd to Qz-Mzn	Hypidiomorphic granular	Qz-Mzd: Pl, Qz, Kfs, Hb, Bt; Mzgr: Pl, Qz, Kfs ↑, Bt, Hbl	Kocatürk, et al. [14]
	North Tepeldağ	Qz-Di to Grd	Porphyritic	Qz-Di: Pl, Qz ↓, Hb, Bt, Kfs ↓; Grd: Pl, Qz, Kfs, Hb, Bt	Altunkaynak, et al. [29]
Gürgenyayla	Main Body	Grd to Mzgr	Hypidiomorphic granular	Grd: Pl, Qz, Kfs, Hb, Bt; Mzgr: Pl, Qz, Kfs ↑, Bt, Hb	Altunkaynak, et al. [29]

Abbreviations: Granodiorite (Grd), Quartz-Monzodiorite (Qz-Mzd), Quartz-Monzonite (Qz-Mzn), Tonalite (Ton), Alkali-Feldspar Granite (Afs-Gr), Quartz-Diorite (Qz-Di), Monzogranite (Mzgr). Pl (Plagioclase), Qz (Quartz), Kfs (K-feldspar), Hbl (Hornblende), Bt (Biotite), Ms (Muscovite), ↑ (higher abundance), ↓ (lower abundance).

3. Methodology

A total of 89 rock- and ore-related samples were systematically collected from four principal domains within the study area. These include (i) the Kirazgedik porphyry Cu-Mo system, spatially and genetically associated with the South Tepeldağ Pluton; and (ii) the Güneybudaklar, (iii) Kozbudaklar, and (iv) Delice regions, which collectively delineate the Nilüfer Mineralization Complex (NMC) and exhibit strong spatial and genetic associations with the Topuk Pluton. The sampling strategy was designed to encompass the full range of mineralization styles and associated lithological environments across these distinct mineralized centers. Targeted lithologies included multiphase intrusive rocks, hydrothermal alteration zones, skarn bodies, and ore-bearing structures such as veins, breccias, and mineralized intrusive contacts. Sampling was conducted along center-to-margin transects within each intrusive body to assess spatial variations in magmatic evolution and subsequent hydrothermal alteration. All collected samples were initially examined petrographically. Based on petrographic and textural criteria, a subset of 29 representative samples was selected for comprehensive analytical work. This included ore mineralogy, whole-rock geochemistry, electron probe microanalysis (EPMA) of amphibole and mica, and Re-Os geochronology of molybdenite-bearing samples.

The analytical data are summarized in the following data products:

- **Supplementary Table S1** details metadata for the 29 representative samples, including sample codes, lithological classifications, spatial information, and associated analytical datasets.
- **Supplementary Table S2** presents whole-rock geochemical data (major oxides and trace elements, including REEs) for the 29 representative samples.
- **Supplementary Table S3** reports ore element concentrations (Cu, Mo, W, Au, Ag, Bi, As, Te, Sb, Sn, Zn, Pb, Re) for the full set of 89 samples.
- **Supplementary Tables S4 and S5** provide quantitative EPMA results for mica and amphibole, respectively, from selected representative samples.
- **Supplementary Figures S1–S4** include representative back-scattered electron (BSE) images of amphibole and mica grains from across each study sector.
- **Table 2** presents the Re-Os isotopic data and corresponding model age for a molybdenite-bearing sample from the Güneybudaklar mineralization.

Table 2. Re–Os isotopic data and model age for molybdenite from the Güneybudaklar porphyry-skarn, with analytical uncertainties reported at the 2σ confidence level.

Re (ppm)	± 2α	^{187}Re (ppb)	±2α	^{187}Os (ppb)	±2α	Model Age (Ma)	±2α with Decay Const (Ma)
34.65	0.10	21,780	61	18.125	0.011	49.93	0.21

3.1. Whole-Rock Geochemical Analysis (XRF & ICP-MS)

Whole-rock geochemical analyses were carried out on all collected samples to determine major, trace, and REE elements concentrations. Major oxides were analyzed by X-ray fluorescence (XRF) using fused bead methods, while trace and precious metals, including REEs, Au, and Ag, were quantified via inductively coupled plasma mass spectrometry (ICP-MS). Trace element determinations followed lithium metaborate fusion and nitric acid digestion. Analyses were conducted at the Geochemistry Research Laboratory (ITU/JAL) of Istanbul Technical University. Certified reference materials and internal standards were employed for calibration and quality control, ensuring high analytical precision and reproducibility.

3.2. Electron Probe Micro-Analysis (EPMA)

Mineral chemical compositions of amphibole and mica were determined through EPMA using a JEOL JXA-8900R electron microprobe (JEOL Ltd., Tokyo, Japan) at the University of Alberta's Electron Microprobe Laboratory. A total of 148 point analyses were conducted on 35 amphibole grains, and 130 point analyses were performed on 21 mica grains, with $\geq$3 analyses per grain to capture intra-grain compositional variation. Analyses were conducted on carbon-coated, polished thin sections under operating conditions of 15 kV accelerating voltage, 30 nA beam current, and a 2 µm beam diameter in spot mode. Major elements were analyzed with 20 = second peak and background counting times; fluorine (F) was analyzed with extended 40 s counting to enhance detection sensitivity. Calibration employed high-purity mineral standards: rutile (Ti), diopside (Mg), plagioclase (Si, Al, and Ca), fayalite (Fe), sanidine (K), tugtupite (Na, Cl), spessartine (Mn), magnesium fluoride (F), sanbornite (Ba), and chromium oxide (Cr). For F and Cl, relative uncertainties approached 5% due to their lower concentrations in mica. BSE imaging guided the selection of homogenous, unaltered grains for analysis.

3.3. Re-Os Geochronology

To constrain the timing of mineralization, a molybdenite-bearing sample was selected from a skarn zone at the northern contact of the Topuk Pluton, where quartz monzonitic

intrusions intersect metagabbroic basement. Among all skarn-hosted domains in the NMC, the Güneybudaklar sector exhibited the highest molybdenum content (>4000 ppm Mo), making it the optimal candidate for Re-Os dating. Approximately 80 mg of molybdenite was isolated through metal-free mechanical separation techniques, including crushing, sieving, magnetic separation, and gravity concentration. Re-Os isotope analyses were conducted at the Crustal Re-Os Geochronology Laboratory (University of Alberta), following established procedures described in Selby and Creaser [30] and Markey et al. [31]. A mixed ^{185}Re–^{190}Os–^{188}Os double-Os spike was used for isotope dilution analyses. Molybdenite digestion, Re-Os separation, and purification were conducted using inverse aqua regia, solvent extraction, and ion exchange chromatography. Isotopic ratios were measured by negative thermal ionization mass spectrometry (NTIMS) using a ThermoScientific Triton instrument (Thermo Fisher Scientific Inc., Waltham, MA, USA). Procedural blanks were <3 pg for Re and <1 pg for Os and are considered negligible. Analytical accuracy was verified using the 8599 Henderson molybdenite standard (27.78 ± 0.07 Ma; Markey et al. [31]), yielding data consistent with the certified age. Age calculations used a ^{187}Re decay constant of 1.666×10^{-11} yr^{-1} [32]. The Re-Os geochronological result is presented in Table 2, summarizing the isotopic composition and model age.

4. Results

4.1. Ore Geology

The NMC comprises a variety of several ore deposit types, including porphyry, skarn, and vein-style mineralization, all situated within a structurally controlled intrusive pathway. In the current study, several mineralization types have been studied in detail, such as Kirazgedik Cu-Mo ± Au porphyry, Güneybudaklar Mo Porphyry-Skarn, Kozbudaklar W–Mo Skarn, and Delice W ± Fe ± Cu Skarn mineralization (Figure 2).

4.1.1. Kirazgedik Cu-Mo ± Au Porphyry Mineralization

The Kirazgedik Cu-Mo ± Au deposit is in northwest Turkey within the Tavşanlı Zone of western Anatolia, which forms part of the Western Tethyan metallogenic belt. This region experienced significant magmatic activity during the Eocene, represented by the South Tepeldağ pluton (U-Pb zircon ages of 54.56 ± 0.21 Ma), attributed to the closure of the Neo-Tethyan ocean and related slab dynamics [9,12,14]. The Eocene intrusions developed within a post-subduction extensional tectonic regime, associated with slab rollback of the subducting Tethyan slab rather than a sudden slab rollback. This tectonic setting marks a transition from subduction-related compression to transtensional deformation during the waning stages of Neo-Tethyan convergence [9]. As a result, a belt of granitic to dioritic stocks was emplaced throughout NW Anatolia, associated with numerous porphyry and skarn mineral deposits [5,6,12]. Kirazgedik mineralization is spatially associated with the South Tepeldağ Pluton, occurring near its eastern and southern margins (Figure 2). This porphyry Cu-Mo ± Au mineralization is hosted by the Eocene South Tepeldağ porphyritic quartz-monzonite to porphyritic quartz diorite intrusion and its surrounding older metamorphic wall rocks (Figures 2 and 3a,b).

Field observations at Kirazgedik reveal that intense hydrofracturing within the apical region of the South Tepeldağ porphyritic stock facilitated the development of a stockwork vein system and breccia zones, which host the principal Cu-Mo mineralization. This ore-bearing zone is centered on the intrusion, where pervasive fracturing and hydrothermal brecciation generated a dense network of quartz-sulfide veins and veinlets that extensively penetrate both the stock and the surrounding country rocks (Figure 3a,b).

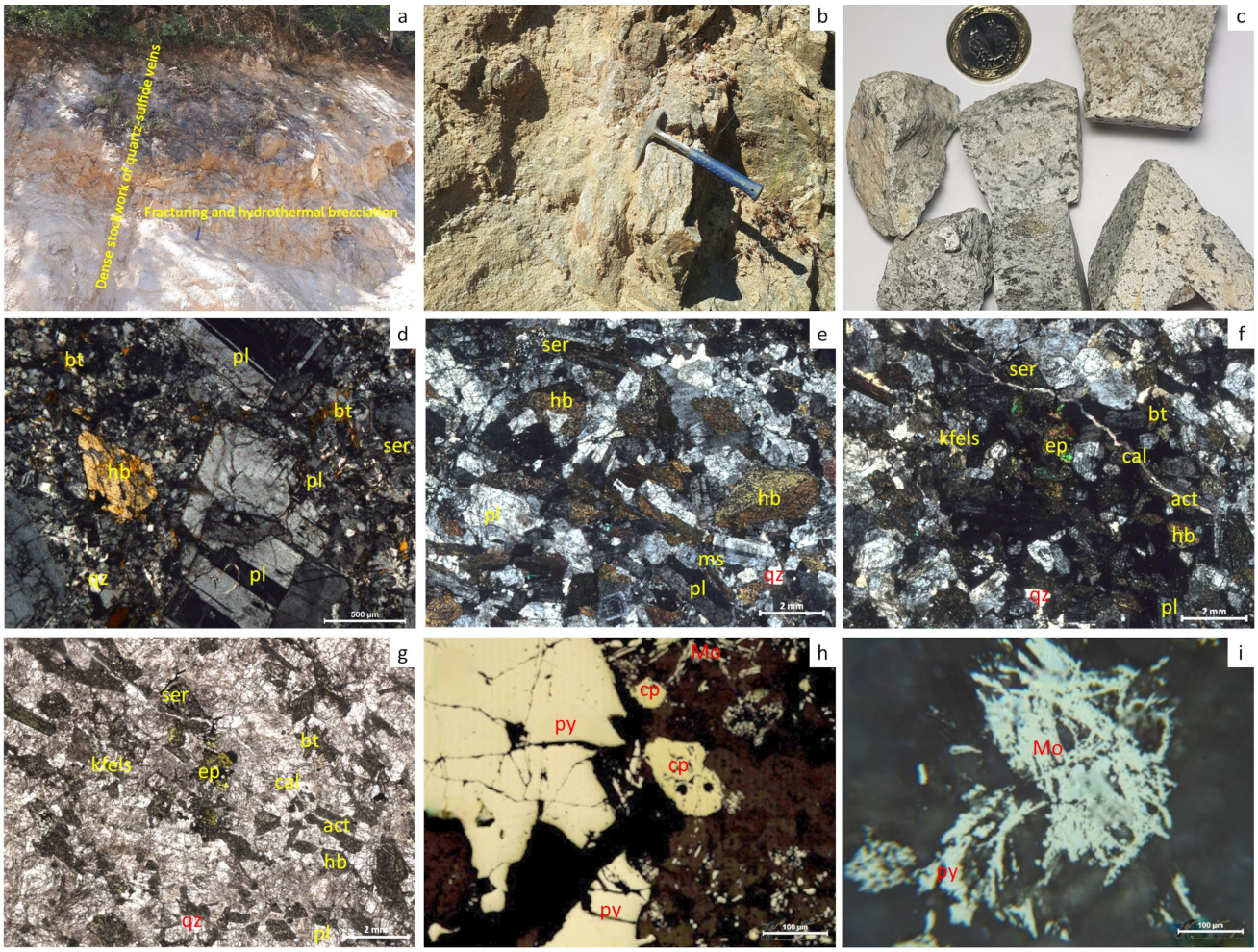

Figure 3. Field, macroscopic, and microscopic investigations of the Kirazgedik Cu-Mo ± Au porphyry mineralization: (**a**,**b**) Pervasive fracturing and hydrothermal brecciation with network of quartz-sulfide veins and veinlets in the South Tepeldağ Pluton. (**c**) Macroscopic view of the porphyritic quartz-monzonite and porphyritic quartz diorite of the South Tepeldağ Pluton. (**d**) Plagioclase (pl) phenocrysts within a medium-grained microcrystalline matrix composed of plagioclase (pl) laths, hornblende (hb), biotite (bt), quartz (qz), and opaque minerals in the porphyritic quartz-monzonite. (**e**) Hornblende (hb) and plagioclase (pl) phenocrysts embedded in medium-grained microcrystalline matrix of plagioclase (pl), muscovite (ms), actinolite (act), quartz (qz) in the porphyritic quartz-diorite. (**f**,**g**) Quartz (qz), K-feldspar (kfels), secondary biotite (bt), sericite (ser), epidote (ep), and calcite veinlet (cal) are the alteration products in the Kirazgedik area. (**h**,**i**) Pyrite (py), chalcopyrite (cp), and molybdenite (Mo) are the main ore minerals that occurred in the Kirazgedik mineralization. The data are taken from Kocatürk [9] and Kocatürk, et al. [14].

Microscopically, the porphyritic quartz-monzonite consists predominantly of plagioclase phenocrysts, some of which are partially sericitized, set within a medium-grained microcrystalline matrix composed of plagioclase laths, hornblende, biotite, quartz, and opaque minerals. (Figure 3c,d). While the porphyritic quartz-diorite is mainly composed of hornblende and plagioclase phenocrysts embedded in a medium-grained microcrystalline matrix of plagioclase, muscovite, actinolite, quartz, and opaque minerals (Figure 3c,e). Gangue minerals include quartz (ubiquitous in all vein types) with the hydrothermal alteration minerals like K-feldspar and secondary biotite (within potassic alteration zones), sericite, and epidote with carbonates (locally in veins or late-stage fractures) (Figure 3f,g).

The dominant ore minerals are chalcopyrite and molybdenite, accompanied by abundant pyrite (Figure 3h,i). Chalcopyrite serves as the principal copper-bearing mineral,

occurring in quartz veinlets and disseminations, whereas molybdenite appears as flakes and rosettes along late quartz veins or vein margins (Figure 3h,i). Geochemical analyses reveal that the Cu concentration in the altered sample reaches up to 1276 ppm, while Mo attains levels as high as 194.1 ppm (Supplementary Table S3). Although gold is not visually observable within the sample, geochemical data indicate trace amounts up to 1.1 ppm (Supplementary Table S3). This gold is likely present as submicroscopic inclusions or as an electrum intimately associated with pyrite and chalcopyrite minerals.

4.1.2. Güneybudaklar Mo-W ± Au Porphyry-Skarn Mineralization

The Güneybudaklar molybdenum mineralization is located within the Tavşanlı Zone of NW Turkey, part of a metallogenic belt characterized by Eocene magmatism that followed the Late Cretaceous collision between the Anatolide-Tauride platform and the Pontide (Sakarya) continent [9,14,33]. The deposit lies on the southern flank of Uludağ (Bursa province), where Eocene granitoid intrusions, notably the Topuk plutons, intruded Paleozoic-Mesozoic metamorphic sequences and Triassic carbonate units along the İzmir-Ankara suture zone [33,34]. The principal intrusive body associated with mineralization is the Topuk granite, which has U-Pb zircon ages of 48.71 ± 0.44 Ma [29]. This granite is an elliptical, east-west trending I-type fractured and moderately weathered granitoid that ranges in composition from granodiorite to granite (Figures 2 and 4a) and contains mafic microgranular enclaves, as well as peripheral margins of quartz monzodioritic to monzogabbroic affinity (Figure 4b); it is also crosscut by late-stage aplite dykes.

This pluton intruded a sequence dominated by Triassic İnönü Marble (recrystallized limestone) and other metamorphic lithologies (Figures 2 and 4c), establishing a critical juxtaposition of magmatic heat against reactive carbonate host rocks [34]. Granodiorite generally exhibits a hypidiomorphic granular texture composed of plagioclase feldspar (50%–65%, predominantly oligoclase), quartz (20%–30%), microperthite (<35%), and mafic minerals (5%–15%), primarily hornblende and biotite (Figure 4d). The monzogabbro enclave comprises approximately equal proportions of plagioclase (labradorite) and alkali feldspar (microperthite and orthoclase), in addition to mafic minerals, predominantly pyroxene (usually clinopyroxene) (Figure 4e).

The Mo-W ± Au mineralization at the Güneybudaklar mineralization is intimately linked both spatially and genetically to the metasomatic contact zone between the Topuk granodiorite intrusion and the surrounding Triassic İnönü Marble. This lithological boundary provides an ideal setting for skarn development due to the contrasting chemical reactivity and permeability between the silica-rich intrusive body and the carbonate host rock, resulting in the formation of both endoskarn within the intrusion and exoskarn in the adjacent marble (Figure 4c,f). Structural discontinuities, notably concentric and radial fractures related to pluton emplacement, acted as conduits for high-temperature magmatic-hydrothermal fluids. These structures, combined with lithological contacts, controlled fluid pathways and localized ore deposition (Figure 4a,c,f). A well-developed skarn system, characterized by a porphyry-style mineralized core having quartz-molybdenite veins in fractures, creating a proto-ore zone rich in molybdenum (and minor copper and gold) (Figure 4g), grading outward into a skarn shell hosted by the marble, forming garnet-rich (completely altered to epidote) and diopside-rich exoskarn zones with minor actinolite (Figure 4h,i). Ore mineralization aligns with this zonation pattern. Molybdenite occurs as veinlets and disseminations within the endoskarn and skarn, typical of the porphyry-style core (Figure 4g,j). Scheelite, often containing a powellite component due to Mo substitution, predominates in the outer skarn zones in which scheelite and powellite's characteristic bireflectance and internal reflections are found (Figure 4k). Retrograde alteration is evidenced by quartz-epidote (Figure 4h) and late-stage sulfide mineralization, including pyrite

(Figure 4l). These late hydrothermal events introduced minor gold mineralization, typically hosted in quartz-sulfide veins crosscutting earlier skarn textures. In addition to the most extreme Mo-enriched sample (4032 ppm), W values as high as 866 ppm and the highest Au observed in the dataset (4.58 ppm), Te and Bi reach 97.8 ppm and 735 ppm, respectively, indicating a volatile-rich late-stage fluid signature (Supplementary Table S3).

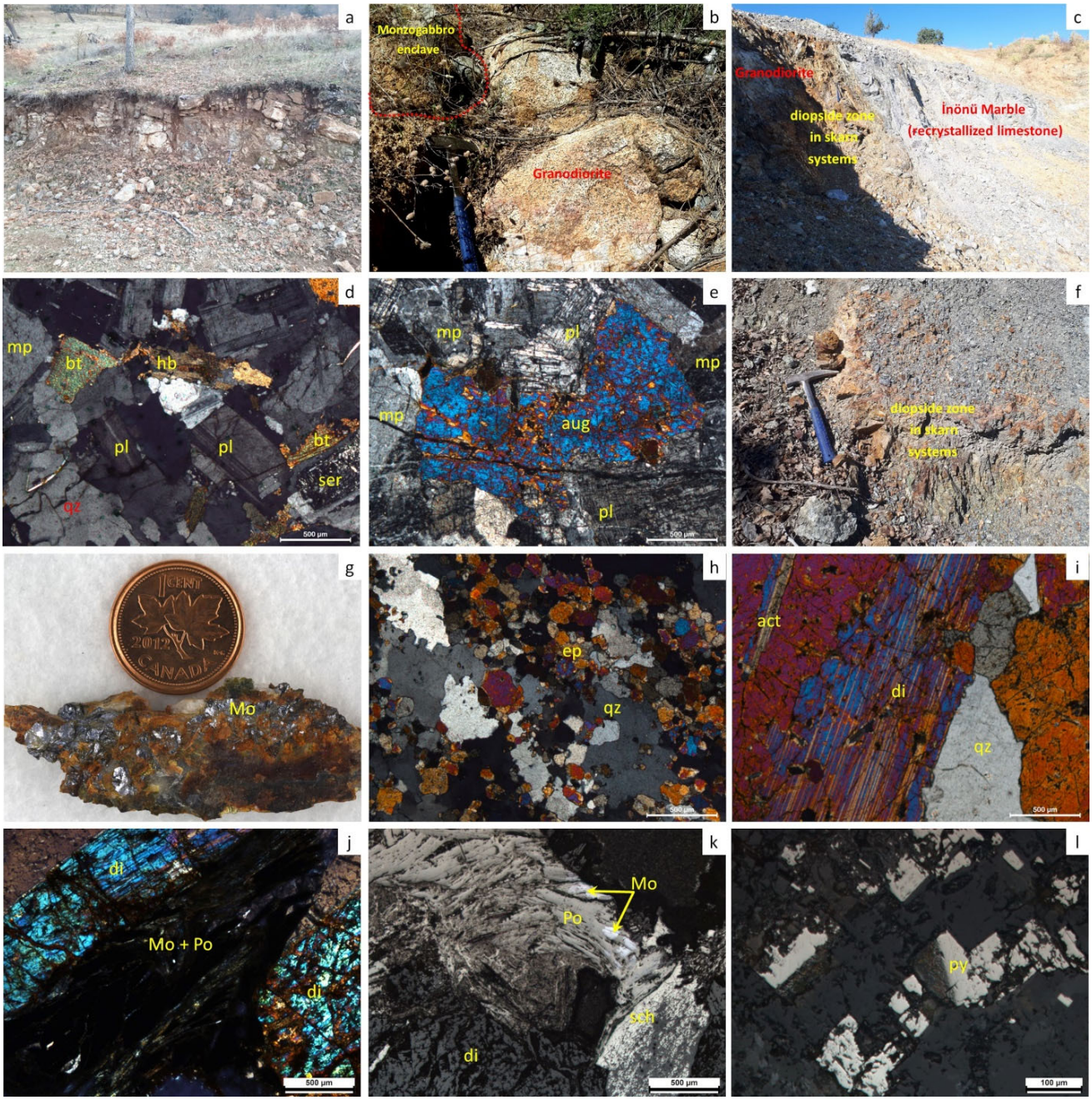

Figure 4. Field, macroscopic, and microscopic investigations of the Güneybudaklar Mo-W ± Au porphyry-skarn mineralization: (**a**) Fractured and moderately weathered Topuk granitoid rock. (**b**) Mafic microgranular enclaves and peripheral margin of monzogabbro within the Topuk granitoid rock. (**c**) Metasomatic contact between Triassic İnönü Marble and Topuk granitoid rock. (**d**) Plagioclase (pl), quartz (qz), microperthite (mp), biotite (bt), and hornblende (hb) in the granodiorite of the Topuk pluton. (**e**) Plagioclase (pl) and microperthite (mp) with augit (aug) in the monzogabbro. (**f**) Diopside

zone in the skarn system along the metasomatic contact between Triassic İnönü Marble and Topuk granitoid rock. (**g**) Molybdenite (Mo)-rich ore with weathered iron-stained quartz matrix. (**h**) Garnet-rich skarn zone that completely altered to epidote (ep) associated with quartz (qz). (**i**) Diopside (di), quartz (qz), and actinolite (act) in the diopside-rich skarn zone. (**j**) Molybdenite (Mo) within diopside (di), typical of the porphyry-style core. (**k**) Molybdenite (Mo) mostly altered to powellite (po) associated with scheelite (sch). (**l**) Pyrite (py) occurred within quartz-epidote during the late-stage sulfide mineralization. The data are taken from Kocatürk [9] and Kocatürk, et al. [14].

4.1.3. Kozbudaklar W ± Mo Skarn Mineralization

The Kozbudaklar W ± Mo skarn deposit, located southeast of Bursa in northwestern Turkey, is hosted within the Triassic İnönü Marble of the Tavşanlı Zone, a metamorphic unit of the northern margin of the Anatolide block formed during Neo-Tethys closure [13,34]. During the Eocene, magmatism, interpreted as post-subduction in origin but commonly referred to as post-collisional in the regional literature, was triggered by slab rollback or progressive slab detachment following the cessation of Neo-Tethyan subduction. This magmatic activity led to the emplacement of the Topuk Pluton and the development of associated skarn systems (e.g., the Eğrigöz, Orhaneli, and Kestanbol plutons) [35,36]. The Topuk Pluton is represented by a medium- to coarse-grained, calc-alkaline, metaluminous I-type granodiorite [14]. Geochemical and petrologic evidence, including mafic micro-granular enclaves of monzogabbro (Figure 4b), indicates magma mixing and mantle-crust interaction typical of volcanic-arc or collision settings. The pluton intruded the marble along a structurally weakened suture zone, causing contact metamorphism and extensive metasomatism that formed the Kozbudaklar skarn (Figure 5a,b). The skarn occurs along the pluton-carbonate contact, varying in thickness up to 850 m, and reflects a collision-related skarn system where magmatic heat and fluids metasomatized older carbonate strata, enabling W ± Mo mineralization [33,34].

The Kozbudaklar skarn W ± Mo mineralization developed both within the marble as exoskarn and within the granitoid as endoskarn adjacent to this contact (Figure 5a,b). The endoskarn is spatially restricted to the margin of the pluton and is characterized by metasomatic replacement of the granite, primarily by plagioclase and pyroxene minerals (Figure 5c). The exoskarn extends outward into the marble, displaying a clear mineralogical zoning with increasing distance from the intrusive contact. In the immediate contact zone, the skarn is dominated by clinopyroxene-rich assemblages composed mainly of diopsidic clinopyroxene with subordinate andradite garnet (Figure 5d,e). Moving further from the contact, the skarn transitions into garnet-rich lenses along the roof and walls of the pluton, composed predominantly of andradite garnet (partly altered to epidote) and calcite (Figure 5f,g). Scheelite, the primary ore mineral, is disseminated throughout these prograde zones during the initial stage of mineralization (Stage 1) (Figure 5h,i). In the subsequent late prograde stage (Stage 2), the skarn assemblage becomes more oxidized, indicative of elevated oxygen fugacity conditions. Scheelite continued to precipitate during this stage but became notably enriched in molybdenum, containing 7%–32% powellite component in solid solution, which imparts the W ± Mo character to the deposit [13]. Molybdenum is predominantly incorporated into scheelite as a solid solution rather than forming abundant discrete molybdenite minerals, which are scarce or absent in the deposit. Kozbudaklar displays the greatest W variability, ranging from 99 to 2558 ppm, at generally low Mo but locally elevated Au (such as 2.09 ppm), consistent with W-rich skarn mineralization (Supplementary Table S3).

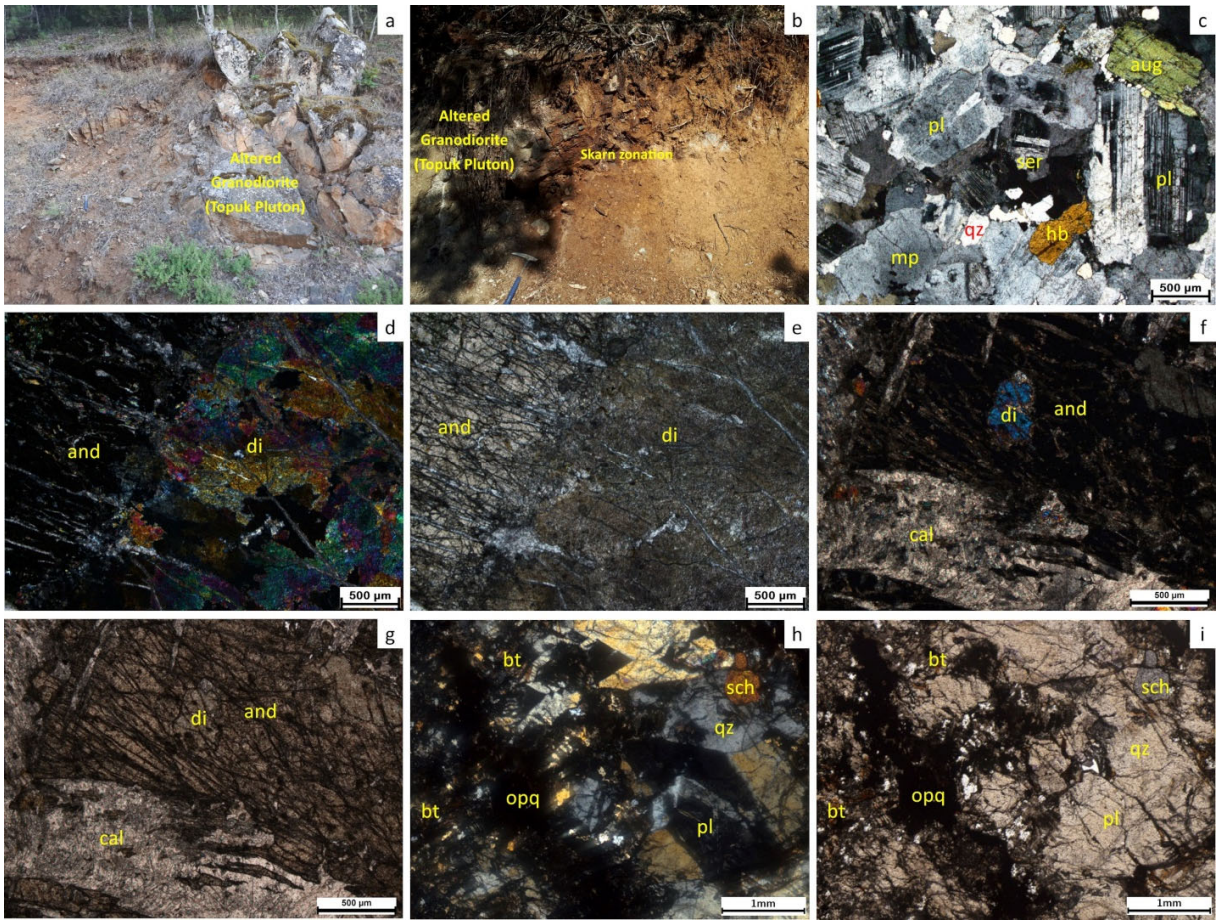

Figure 5. Field, macroscopic, and microscopic investigations of the Kozbudaklar W ± Mo skarn mineralization: (**a**) Altered granodiorite (Topuk pluton) at Kozbudaklar W ± Mo skarn deposit area. (**b**) Extensive contact metasomatism along the structurally weakened suture zone forming the Kozbudaklar skarn mineralization. (**c**) Endoskarn primarily formed from plagioclase (pl) and augite (aug) in the altered granodiorite having quartz (qz), microperthite (mp), sericite (ser), and hornblende (hb). (**d**,**e**) Diopside (di) and andradite (and) in the clinopyroxene-rich exoskarn zone. (**f**) and (**g**) Andradite (and) and calcite (cal) with little diopside (di) in the exoskarn garnet-rich zone. (**h**,**i**) disseminated scheelite (sch) throughout the prograde zones with the altered plagioclase (pl), biotite (bt), quartz (qz), and opaque minerals (opq).

4.1.4. Delice W ± Fe ± Cu Skarn Mineralization

The Delice W ± Fe ± Cu skarn deposit is located in the Tavşanlı Zone, a metallogenic belt characterized by Eocene magmatic activity, in northwest Turkey, south of Uludağ Mountain in Bursa Province [9]. The mineralization is genetically linked to Eocene magmatism (≈54 to 45 Ma), which occurred in a post-subduction extensional setting [9,14]. The mineralization formed at the contact between the Topuk Pluton, a zoned, calc-alkaline, I-type granitoid, and the Triassic İnönü Marble Formation (Figure 6a). The Topuk intrusion comprises tonalite-granodiorite to alkali-feldspar granite with mafic enclaves and late-stage granite-aplite dikes (Figure 6b). Tonalite and tonalite porphyry are the main stock of Topuk granite, having mainly plagioclase phenocrysts embedded in a microcrystalline matrix of plagioclase, quartz, biotite, and hornblende with minor microperthite and opaques (Figure 6c). U-Pb zircon ages date the pluton between 47.3 ± 0.2 Ma and 45.9 ± 0.3 Ma, placing mineralization firmly in the mid-Eocene [9,14]. Sr-Nd isotopes ($^{87}Sr/^{86}Sr \approx 0.706–0.707$, $\varepsilon Nd \approx -2$ to -4) confirm a mantle-derived magma with significant crustal interaction [9,13,14].

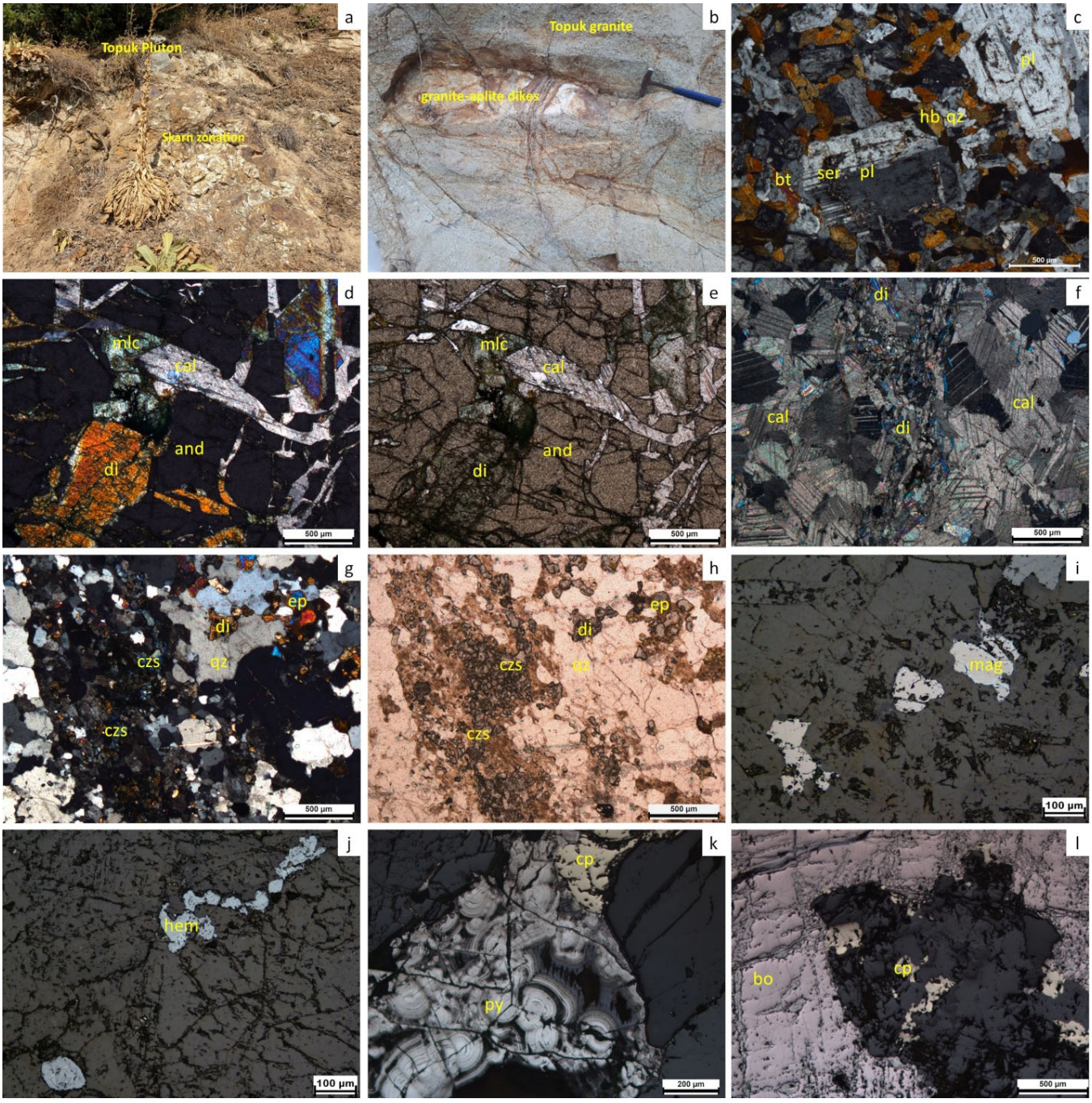

Figure 6. Field, macroscopic, and microscopic investigations of the Delice W ± Fe ± Cu skarn mineralization: (**a**) Metasomatic contact between the Topuk Pluton and Triassic İnönü Marble Formation at Delice. (**b**) Late-stage granite-aplite dikes cut through Topuk granite. (**c**) Plagioclase (pl) phenocrysts are embedded in a microcrystalline matrix of plagioclase (pl), quartz (qz), biotite (bt), and hornblende (hb) with minor sericite (ser) and opaques in tonalite porphyry. (**d**,**e**) Andradite (and) and diopside (di) with calcite (cal) in the prograde metasomatic alteration, forming calc-silicate skarn and latterly having malachite (mlc). (**f**) Diopside (di) formed within the calcite (cal) of the İnönü Marble Formation. (**g**,**h**) Epidote (ep), clinozoisite (czs), chlorite, and sericite within quartz (qz) occurring within the retrograde metasomatic alteration. (**i**) Idiomorphic to subhedral grains of magnetite (mag) formed in the early skarn stages. (**j**) Minor hematite (hem) occurs, reflecting locally variable oxidation states. (**k**) Colloform pyrite (py) occurred with chalcopyrite (cp). (**l**) Bornite (bo) occurred with chalcopyrite (cp).

The deposit exhibits a well-defined contact-metasomatic system. Skarn formation occurred as magmatic-hydrothermal fluids emanating from the Topuk Pluton penetrated the adjacent carbonate host along fractures, bedding planes, and fold hinges (Figure 6a). These fluids induced prograde metasomatic alteration, forming calc-silicate skarn composed of garnet (andradite) and pyroxene (diopside-hedenbergite) (Figure 6d–f). As the system cooled and fluids evolved, retrograde alteration overprinted the prograde skarn. This introduced amphiboles (tremolite-actinolite), epidote-clinozoisite, chlorite, and sericite, replacing earlier garnet and pyroxene, commonly associated with tungsten (scheelite) precipitation during fluid cooling and structural fracturing (Figure 6g,h). Mineralogically, scheelite is the principal tungsten ore mineral at Delice. It is disseminated in the skarn matrices and in cross-cutting veins. Importantly, relict wolframite is also found, primarily in the contact zone, partially replaced by scheelite, indicating an evolution from a more reduced, Fe-rich fluid to a more oxidized one. In terms of iron minerals, magnetite is abundant, especially in the early stage, where it can form idiomorphic to subhedral grains (Figure 6i). Minor hematite also occurs, and conversely some pyrrhotite is present, reflecting locally variable oxidation states (Figure 6j). Pyrite is the most widespread sulfide mineral, occurring throughout both the contact zone and the skarn (Figure 6k). However, other base-metal sulfides are more confined to the distal skarn lenses away from the contact, including chalcopyrite with bornite (Figure 6l). Malachite is represented by supergene minerals after Cu-bearing minerals (Figure 6d,e). Delice samples combine high W, peaking at 2391 ppm in D29, with notable Bi, 941 ppm in D28, and appreciable Au up to 1.22 ppm (Supplementary Table S3).

4.2. Whole-Rock Geochemistry

Whole-rock major and trace element geochemical data from key intrusive domains were compiled to elucidate the magmatic evolution of the NMC and its adjacent plutonic units. The dataset comprises representative samples from the Kirazgedik, Güneybudaklar, Kozbudaklar, and Delice sectors, each selected to capture distinct intrusive phases and stages of magmatic differentiation. Although the Kirazgedik samples originate from the South Tepeldağ Pluton and are not genetically associated with the NMC, they are included here as a regional compositional reference. All geochemical diagrams were generated using GCDkit software (version 6.0) [37].

Recent petrogenetic interpretations by Kocatürk et al. [14] reclassify the NMC intrusions as genetically linked phases of the Topuk Pluton. In contrast, the Kirazgedik samples represent a compositionally independent magmatic suite and serve as a baseline for evaluating regional geochemical variation. Major and trace element data for the four intrusive sectors were plotted using six geochemical discrimination diagrams (Figure 7a–f) and eight SiO_2-variation plots (Figure 8a–h). On the P–Q diagram (Figure 7a), Kirazgedik samples cluster within the quartz-monzodiorite to quartz-monzonite fields, whereas the Kozbudaklar samples span tonalite, quartz diorite, and granodiorite compositions. Delice samples are mostly confined to the tonalite–quartz diorite field, with a few plotting in the granite field, while Güneybudaklar is entirely represented within the granodiorite field. The SiO_2 versus FeO^t/MgO diagram (Figure 7b) reveals that most of the analyzed samples exhibit a calc-alkaline geochemical affinity, notably those from Kirazgedik, Kozbudaklar, Güneybudaklar, and Delice, with a subset of samples from Güneybudaklar and Delice straddles the transition zone toward tholeiitic compositions. Further insights are provided by the K_2O versus SiO_2 plot (Figure 7c), which classifies the majority of the samples as high-K calc-alkaline, with a few Delice samples extending into the shoshonitic field. Elevated K_2O contents are commonly associated with metasomatized lithospheric mantle sources or assimilation of crustal materials, both of which are frequent in post-collisional orogenic

settings [38,39]. Supporting this interpretation, the CaO–Al_2O_3/(FeO + MgO)–K_2O/Na_2O ternary diagram (Figure 7d) indicates source heterogeneity among the sample groups. Kirazgedik and Kozbudaklar samples tend to cluster within the high-K mafic, suggesting derivation from enriched mantle or lower crustal protoliths, whereas Delice samples show broader dispersion toward the low-K mafic rocks, implying significant crustal assimilation [40,41]. The plot of Dy/Yb versus SiO_2 (Figure 7e) offers further constraints on the depth and residual mineralogy of magma generation. Elevated Dy/Yb ratios in Kirazgedik samples suggest melting in the presence of residual garnet, consistent with a relatively deep lithospheric mantle source (>80 km), where garnet remains stable [42,43]. By contrast, lower Dy/Yb ratios in Güneybudaklar and Kozbudaklar point to melting under shallower conditions, likely involving amphibole as the dominant residual phase, which is typical for crustal or upper lithospheric levels. The Rb versus Y + Nb tectonic discrimination diagram (Figure 7f) places the majority of the samples, especially from Kirazgedik and Kozbudaklar, within the post-collisional granite (post-COLG) field. This tectonic setting is commonly associated with lithospheric thinning and slab rollback following continental collision [44,45]. Meanwhile, several Delice samples fall into the volcanic arc granite (VAG) and syn-collisional granite (syn-COLG) domains, reinforcing a complex magmatic history that includes both subduction-related and post-collisional processes.

Trace-element variation diagrams reveal coherent evolutionary trends. Compatible elements such as Ni and Mg decrease with increasing SiO_2 (Figure 8a,c), with Kirazgedik showing the highest concentrations and Güneybudaklar the lowest. Similarly, V and Sr contents decline with silica (Figure 8b,d); the most pronounced drop in Sr occurs in Güneybudaklar, where concentrations fall below 200 ppm. In contrast, incompatible elements such as Zr and Rb display increasing trends with SiO_2 (Figure 8e,f), attaining their highest levels in Güneybudaklar and, for Zr, also in Kozbudaklar. La exhibits a decrease with silica (Figure 8g), whereas K_2O/Na_2O ratios increase sharply, again culminating in Güneybudaklar (Figure 8h). Together, these diagrams delineate a systematic compositional progression from mafic to felsic lithologies and from low-K to high-K affinity across the four intrusive domains.

Chondrite-normalized REE patterns (Figure 9a–d) exhibit enrichment in light REEs (LREEs) and relatively flat heavy REE (HREE) distributions across all sectors. Kirazgedik samples display moderately fractionated REE patterns with weak negative Eu anomalies. In contrast, Güneybudaklar displays steeper LREE/HREE slopes and more pronounced negative Eu anomalies. Kozbudaklar exhibits moderately sloping REE trends, while Delice is characterized by flatter patterns and variable Eu anomalies, suggesting diverse degrees of plagioclase fractionation and crustal interaction.

Primitive mantle-normalized multi-element diagrams (Figure 9e,h) for all sectors exhibit similar overall patterns—namely enrichment in large-ion lithophile elements (e.g., Rb, Th, Ba) and depletion in high-field-strength elements (e.g., Nb, Ti). Although the general patterns are consistent across the suite, the magnitude of enrichment and depletion varies among the different intrusive sectors, reflecting subtle differences in source composition and magmatic evolution.

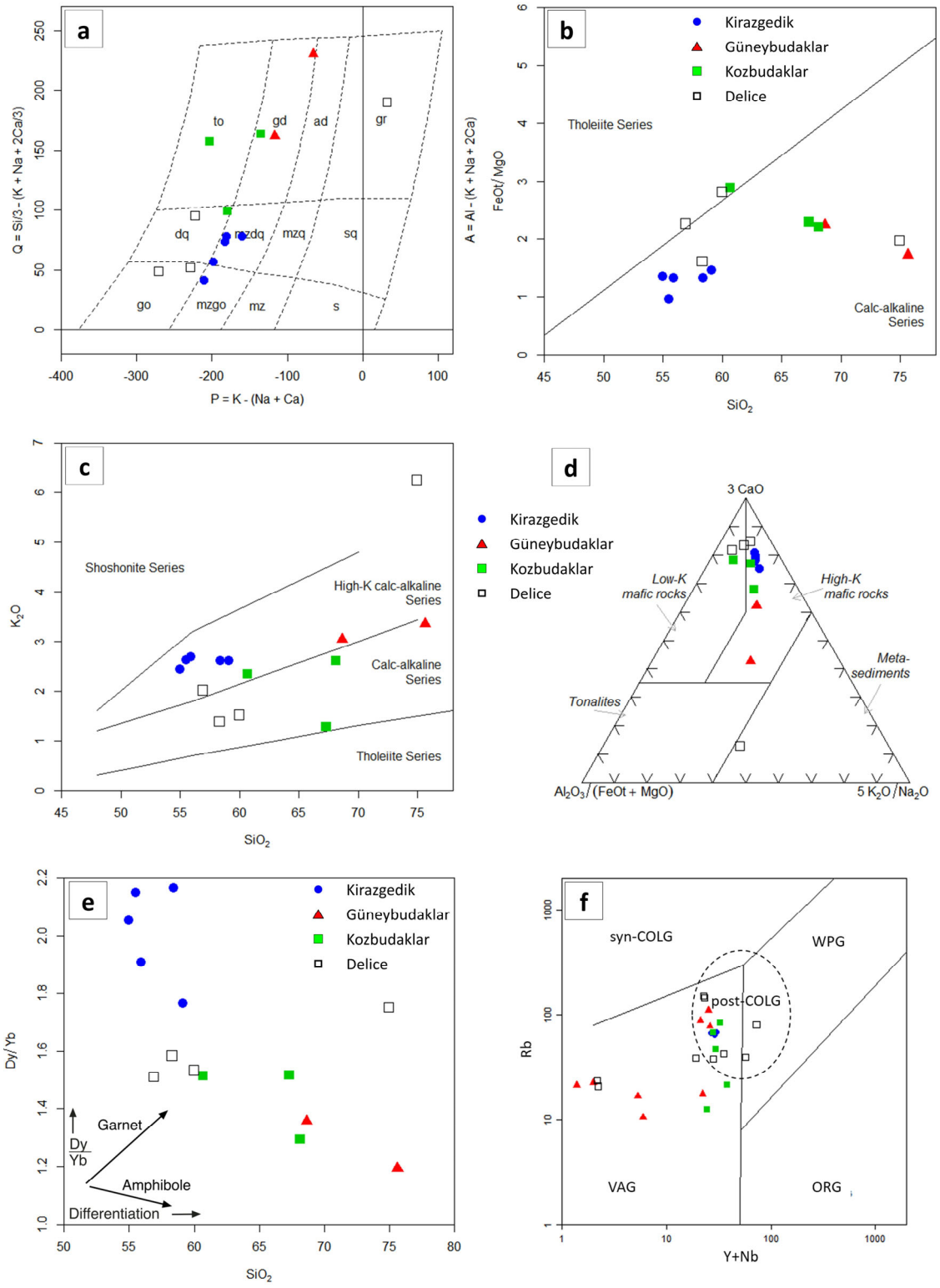

Figure 7. Major and trace element discrimination diagrams for intrusive samples. (**a**) P-Q diagram [46], abbreviations: adamellite (ad), gabbro or diorite (go/di), granite (gr), granodiorite (gd), quartz diorite (qd), quartz monzodiorite (qmzd), quartz monzonite (qmz), quartz syenite (qs), monzodiorite (mzd), monzonite (mz), syenite (s), tonalite (to); (**b**) SiO_2 versus FeO^t/MgO plot [47]; (**c**) K_2O vs. SiO_2 [48]; (**d**) $Al_2O_3/(FeO_t + MgO)$–$3CaO$–$5(K_2O/Na_2O)$ ternary plot for granitoids. The compositions of melts derived from several sources after Laurent, et al. [49]; (**e**) Dy/Yb vs. SiO_2 diagram [42]; (**f**) The Rb-(Y + Nb) diagram [50], Abbreviations: Ocean Ridge Granites (ORG), Within Plate Granites (WPG), Volcanic Arc Granites (VAG), and Syn-and Post-collision Granites (syn-COLG and post-COLG).

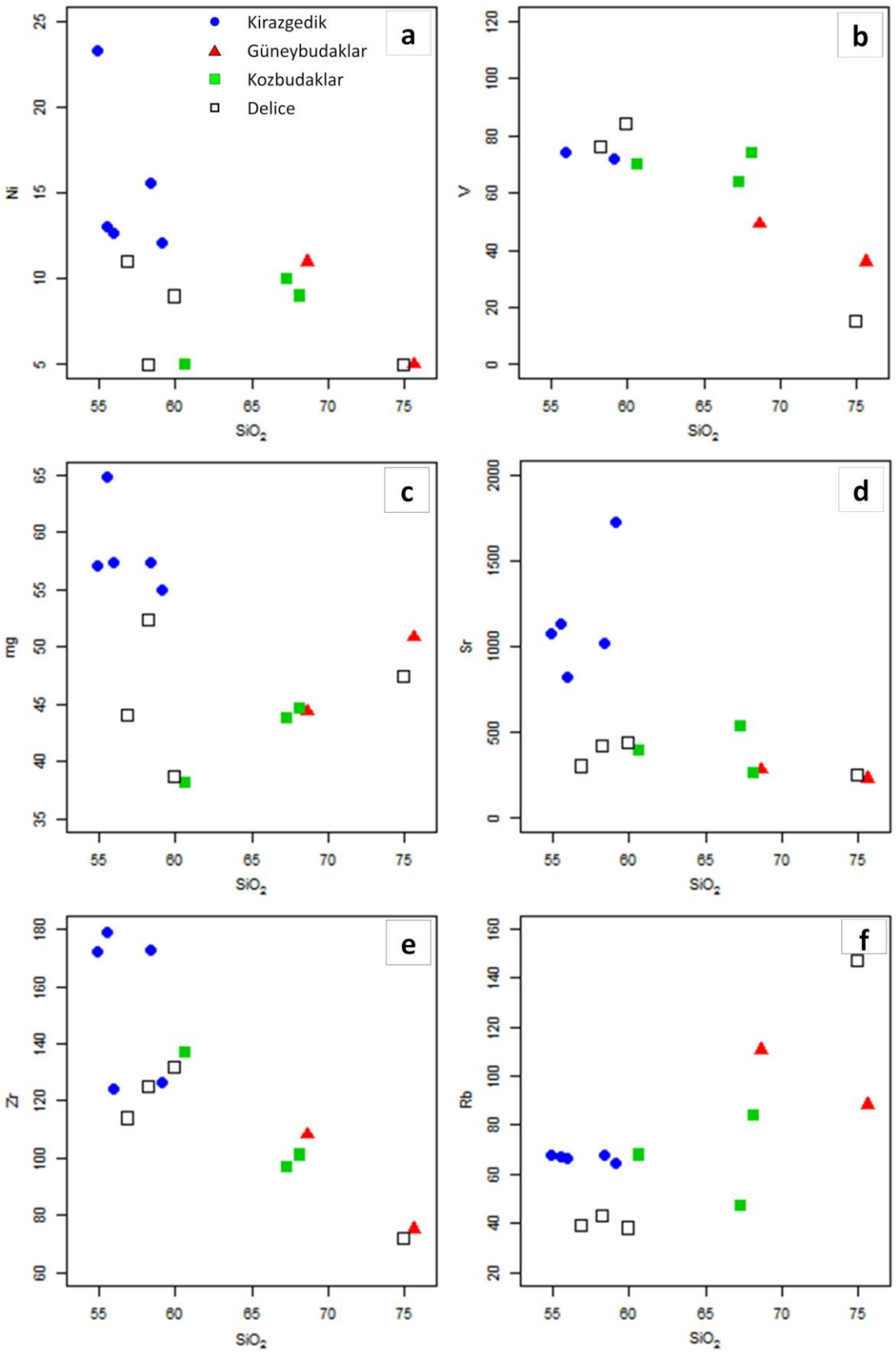

Figure 8. *Cont*.

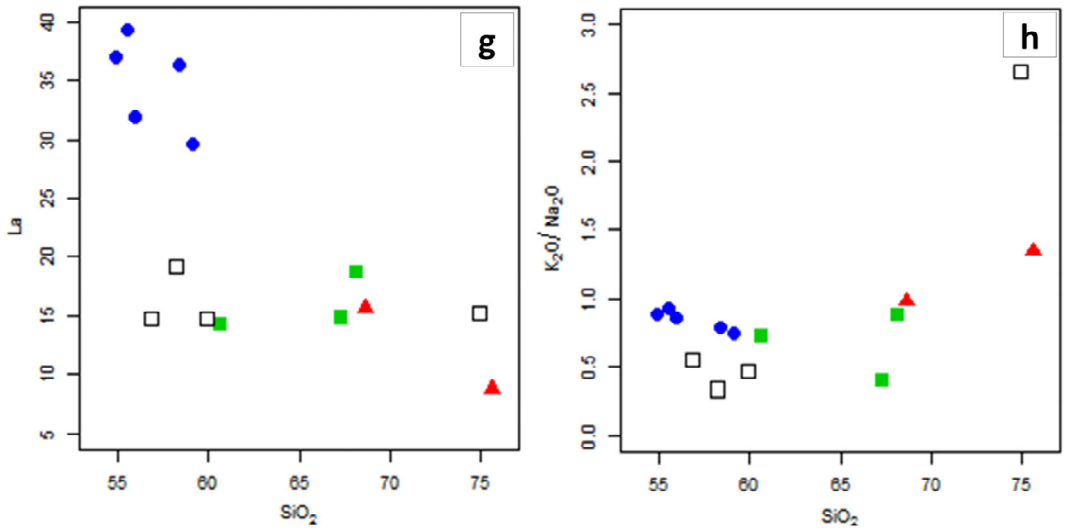

Figure 8. Selected trace element variation diagrams plotted against SiO_2 for samples from Kirazgedik and the three NMC sectors. SiO_2 versus Ni (**a**); V (**b**); Mg (**c**); Sr (**d**); Zr (**e**); Rb (**f**); La (**g**); and K_2O/Na_2O (**h**). Elements include Sr, Rb, Zr, V, and Ni, reflecting magma evolution trends and fractionation behavior. Interpretations follow the approaches of Gill [51], Pearce [52], and Rollinson [40].

4.3. Re–Os Geochronology

Re–Os isotopic dating of molybdenite from the Güneybudaklar skarn zone yields a model age of 49.93 ± 0.21 Ma (2σ). The analyzed sample displays moderate Re concentrations (34.65 ppm) (Table 2).

4.4. Mineral Geochemistry

4.4.1. Mica Geochemistry

Systematic compositional variations in mica across the four studied sectors reflect evolving magmatic conditions and varying degrees of fluid-rock interaction. Major element analyses of biotite display notable inter-sectoral differences. SiO_2 contents range from 33.7 to 40.0 wt.%, with the highest average observed in Kirazgedik (37.9 wt.%) and the lowest in Güneybudaklar (35.0 wt.%) (Table 3). TiO_2 contents peak at 4.3 wt.% in Kozbudaklar and Güneybudaklar, while Kirazgedik biotites show the lowest average (2.9 wt.%) (Table 3). A progressive increase in FeO is evident from Kirazgedik (avg. 12.5 wt.%) through Güneybudaklar (22.0 wt.%) and Kozbudaklar (22.9 wt.%), to a maximum in Delice (24.7 wt.%) (Table 3). Inversely, MgO decreases from 17.3 wt.% in Kirazgedik to 7.8 wt.% in Delice. The Mg number (XMg = Mg/[Mg + Fe], apfu) exhibits a declining trend from Kirazgedik (avg. 0.7) to Delice (avg. 0.4) (Table 3), implying advancing magmatic differentiation and oxidation.

Halogen systematics further discriminate the sector: Fluorine (F) concentrations are highest in Kirazgedik (1.3–1.5 wt.%, avg. 1.4 wt.%), followed by Kozbudaklar (0.4–0.5 wt.%, avg. 0.5 wt.%), Güneybudaklar (0.3–0.7 wt.%, avg. 0.6 wt.%), and the lowest in Delice (0.3–0.4 wt.%, avg. 0.4 wt.%) (Table 3). Corresponding atomic proportions (apfu) support these trends, ranging up to 0.6 apfu in Kirazgedik and from 0.2–0.3 apfu elsewhere. Chlorine (Cl) concentrations remain low and consistently low across all sites (≤0.2 wt.%, ≤0.1 apfu), indicating minimal Cl enrichment (Table 3).

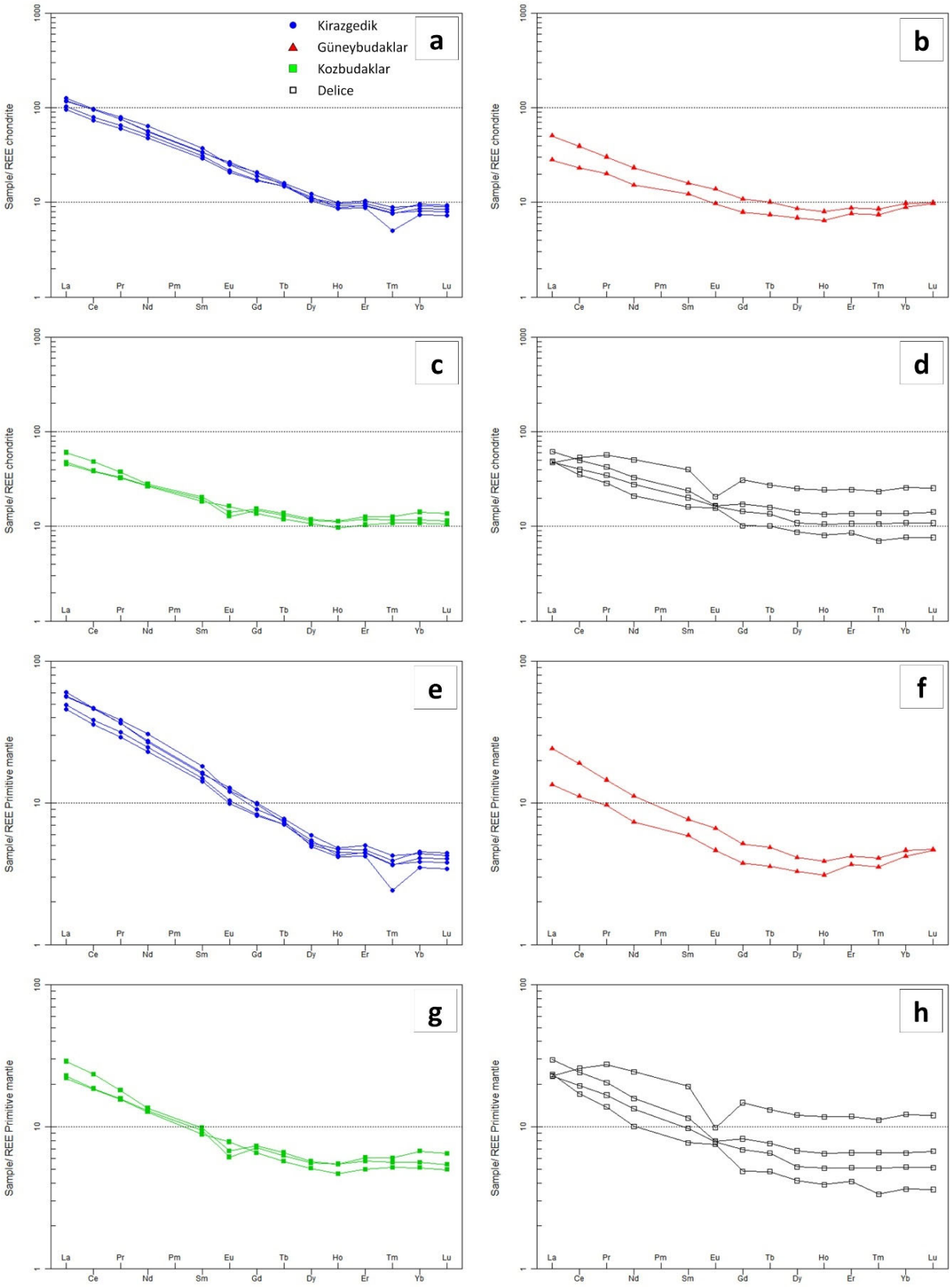

Figure 9. (**a**–**d**) Chondrite-normalized REE patterns for samples from (**a**) Kirazgedik, (**b**) Güneybudaklar, (**c**) Kozbudaklar, (**d**) Delice (normalization values from William and Boynton [53], (**e**–**h**) Primitive mantle-normalized multi-element diagrams for samples from (**e**) Kirazgedik, (**f**) Güneybudaklar, (**g**) Kozbudaklar, (**h**) Delice (normalization values from Sun and McDonough [54]).

Table 3. Summary of mica EPMA analytical results (wt.%).

DataSet	Kirazgedik (*n* = 11)			Güneybudaklar (*n* = 70)			Kozbudaklar (*n* = 15)			Delice (*n* = 34)		
	Min.	**Max.**	**Av.**	**Min.**	**Max.**	**Av.**	**Min.**	**Max.**	**Av.**	**Min.**	**Max.**	**Av.**
SiO_2	35.6	40	37.9	33.7	36.2	35	35	35.6	35.3	34.8	36.2	35.4
TiO_2	2.3	4.2	2.9	2.8	4.3	3.7	3.4	4.3	3.7	3.1	4.1	3.8
Al_2O_3	13.4	14.8	14.2	13.8	16.8	15.6	14	14.4	14.2	13.8	15.1	14.3
FeO	11.6	12.9	12.5	19.2	23	22	22	23.8	22.9	22.8	25.6	24.7
MnO	0.2	0.3	0.2	0.2	0.7	0.3	0.4	0.4	0.4	0.5	0.6	0.6
MgO	16.5	19.7	17.3	7.6	11.5	8.8	8.6	9.6	9.1	6.9	9.4	7.8
CaO	0	3.4	0.4	0	0.1	0	0	0.1	0	0	0	0
Na_2O	0.1	0.3	0.2	0	0.3	0.1	0.1	0.2	0.1	0	0.2	0.1
K_2O	5.6	10.4	9.5	9.4	10.4	9.9	9	10.2	9.9	9.6	10.2	10
Cr_2O_3	0	0.1	0	0	0.1	0	0	0.1	0	0	0.1	0
H_2O *	3.3	3.5	3.4	3.5	3.8	3.6	3.6	3.7	3.6	3.6	3.7	3.7
Li_2O *	0.7	1.9	1.3	0.1	0.8	0.5	0.5	0.7	0.6	0.4	0.9	0.6
F	1.3	1.5	1.4	0.3	0.7	0.6	0.4	0.5	0.5	0.3	0.4	0.4
Cl	0.1	0.2	0.2	0.1	0.2	0.1	0.1	0.2	0.1	0.1	0.2	0.1
Atoms per formula unit (apfu)												
Si	5.3	5.7	5.5	5.3	5.5	5.4	5.5	5.5	5.5	5.4	5.5	5.5
Al^{iv}	2.2	2.5	2.4	2.5	2.7	2.6	2.5	2.5	2.5	2.5	2.6	2.5
Al^{vi}	0	0	0	0	0.5	0.2	0	0.1	0.1	0	0.2	0.1
Ti	0.3	0.5	0.3	0.3	0.5	0.4	0.4	0.5	0.4	0.4	0.5	0.4
Cr	0	0	0	0	0	0	0	0	0	0	0	0
Fe	1.4	1.6	1.5	2.4	3	2.8	2.9	3.1	3	2.9	3.4	3.2
Mn	0	0	0	0	0.1	0	0	0.1	0.1	0.1	0.1	0.1
Mg	3.6	4.3	3.8	1.8	2.6	2	2	2.2	2.1	1.6	2.2	1.8
Ca	0	0.5	0.1	0	0	0	0	0	0	0	0	0
Na	0	0.1	0.1	0	0.1	0	0	0.1	0	0	0.1	0
K	1.1	1.9	1.8	1.9	2.1	2	1.8	2	2	1.9	2	2
F	0.6	0.7	0.6	0.2	0.4	0.3	0.2	0.2	0.2	0.1	0.2	0.2
Cl	0	0	0	0	0	0	0	0.1	0	0	0.1	0
OH *	3.3	3.4	3.3	3.6	3.8	3.7	3.7	3.8	3.7	3.7	3.8	3.8
Li *	0.4	1.1	0.8	0.1	0.5	0.3	0.3	0.4	0.4	0.3	0.5	0.4
TOTAL	19.7	20.4	20.2	19.8	20.1	19.9	19.8	20	20	19.9	20.1	20
Parameters												
Al^{total}	2.2	2.5	2.4	2.5	3.1	2.8	2.5	2.6	2.6	2.5	2.7	2.6
Mg-Li	2.7	3.6	3	1.5	2.1	1.7	1.7	1.8	1.7	1.2	1.7	1.4
Fe + Mn + Ti-Al^{vi}	1.8	1.9	1.9	2.7	3.2	3.1	3.2	3.5	3.4	3.4	3.8	3.6
X(Mg) = Mg/(Mg + Fe)	0.7	0.7	0.7	0.4	0.5	0.4	0.4	0.4	0.4	0.3	0.4	0.4
X(Fe) = Fe/(Fe + Mg)	0.3	0.3	0.3	0.5	0.6	0.6	0.6	0.6	0.6	0.6	0.7	0.6
Fe + Mn	1.5	1.6	1.6	2.5	3	2.9	2.9	3.1	3	3	3.4	3.3
Al^{iv} + Fe + Ti	1.7	1.9	1.8	2.9	3.8	3.5	3.4	3.6	3.5	3.4	3.9	3.7
Fe + Mn + Ti	1.8	1.9	1.9	3	3.5	3.3	3.3	3.6	3.5	3.4	3.9	3.7
FeO/(FeO + MgO)	0.4	0.4	0.4	0.6	0.7	0.7	0.7	0.7	0.7	0.7	0.8	0.8
$TiO_2 \times 10$	23.1	42.3	28.8	27.7	42.7	37.1	33.9	42.7	36.7	30.8	41	37.5
FeO + MnO	11.8	13.1	12.8	19.9	23.2	22.3	22.4	24.2	23.3	23.3	26.2	25.3
ln(Ti)	−1.4	−0.8	−1.2	−1.1	−0.7	−0.8	−0.9	−0.7	−0.9	−1	−0.7	−0.8
T (oC)	497.6	523.2	507.9	269.3	369	296.9	280.4	311	295.7	231.1	303.4	257.1

H_2O *, Li_2O *, OH *, and Li * values are estimated based on stoichiometric calculations.

In Figure 10a, all biotite compositions plot within the Mg–Fe mica compositional field. Kirazgedik biotites classify as Mg-biotite, while Delice, Güneybudaklar, and Kozbudaklar classify as Fe-biotite, consistent with late-stage magmatic evolution. In the $TiO_2 \times 10$–FeO + MnO–MgO ternary diagram (Figure 10b), Kirazgedik biotites fall within the "magmatic and newly formed biotite" field, while samples from other sectors align with the "primary magmatic" field, highlighting fluid-mediated overprinting during later magmatic stages.

Ti-in-biotite thermometry indicates that biotites in Kirazgedik crystallized at the highest average temperatures (avg. ~508 °C), progressively decreasing in Kozbudaklar (~296 °C), Güneybudaklar (~297 °C), and Delice (~257 °C) (Table 3).

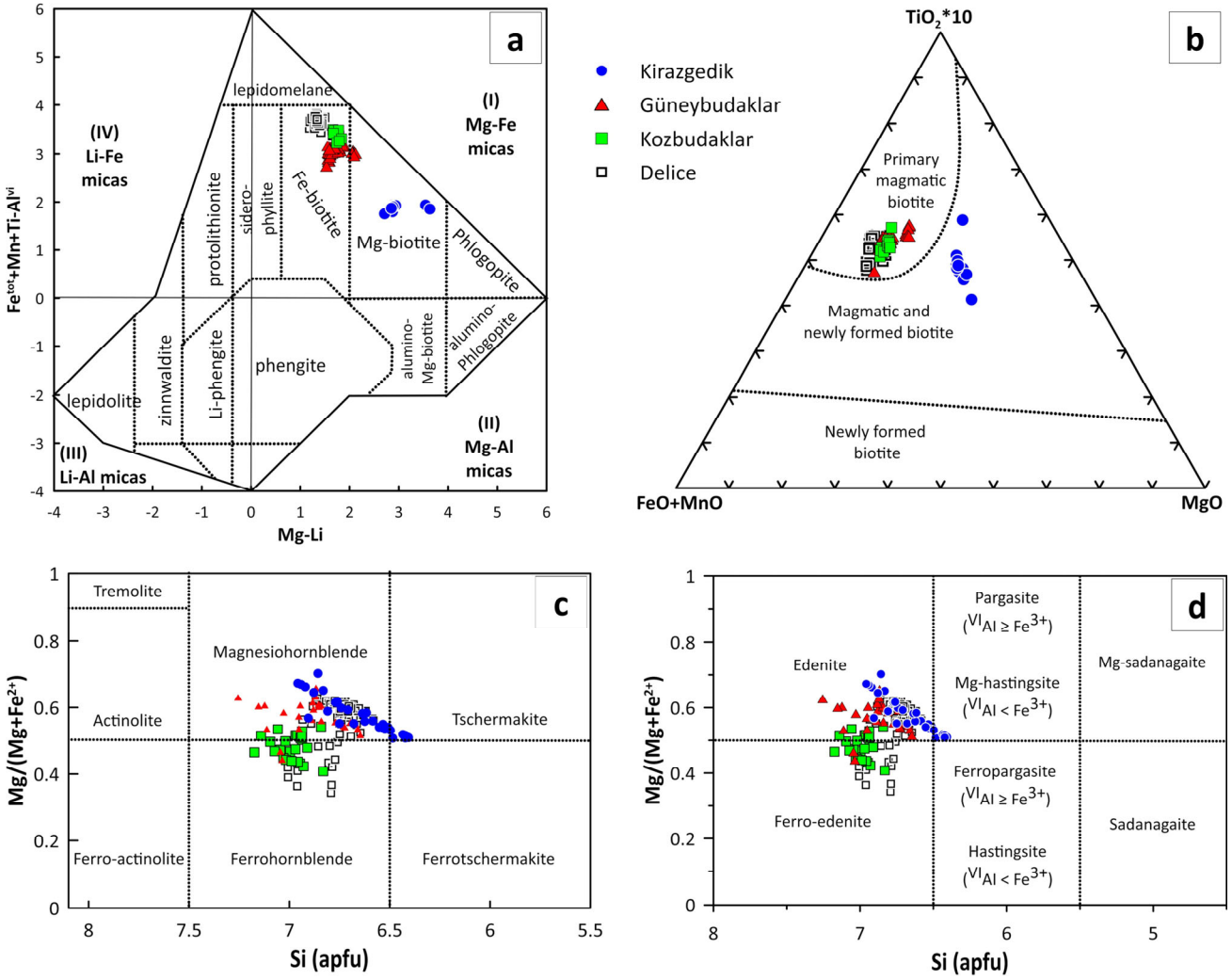

Figure 10. Mineral compositional classification and discrimination diagrams. (**a**) Mica classification in the Fe + Mn + Ti vs. Mg–Li field according to Tischendorf, et al. [55]; (**b**) Biotite typology in the TiO_2 × 10-FeO + MnO-MgO ternary plotm, after Nachit, et al. [56]; (**c**,**d**) Amphibole classification using Mg/(Mg + Fe^{2+}) vs. Si (apfu), after Leake, et al. [57].

4.4.2. Amphibole Chemistry

Amphibole geochemistry similarly reflects inter-sectoral differentiation. SiO_2 content ranges from 42.1 to 49.2 wt.%, with the highest averages recorded in Kozbudaklar (46.3 wt.%) and Güneybudaklar (46.0 wt.%). TiO_2 reaches up to 1.9 wt.%, with Kirazgedik amphiboles averaging the highest values (1.3 wt.%) (Table 4). Al_2O_3 values range from 5.2 to 10.5 wt.% the highest averages in Delice and Kirazgedik (~9.0 wt.%) and the lowest in Kozbudaklar (7.4 wt.%) (Table 4). A systematic increase in FeO is evident from Kirazgedik (avg. 15.7 wt.%) to Delice (avg. 16.5 wt.%) and peaking in Kozbudaklar (avg. 19.3 wt.%) (Table 4). Conversely, MgO decreases from 12.2 wt.% in Kirazgedik to 11.5 wt.% in Delice. MnO values remain low (0.4–1.3 wt.%) across all sectors (Table 4).

Table 4. Summary of amphibole EPMA analytical results (wt.%).

	Kirazgedik (*n* = 28)			Güneybudaklar (*n* = 29)			Kozbudaklar (*n* = 25)			Delice (*n* = 66)		
Dataset	**Min.**	**Max.**	**Av.**	**Min.**	**Max.**	**Av.**	**Min.**	**Max.**	**Av.**	**Min.**	**Max.**	**Av.**
SiO_2	42.1	47.5	44.6	43.8	49.2	46.0	44.5	47.7	46.3	43.5	46.4	45.1
TiO_2	0.8	1.9	1.3	0.4	1.5	1.0	0.5	1.0	0.8	0.7	1.3	1.1
Al_2O_3	7.5	10.4	9.1	5.2	9.5	8.0	5.9	8.7	7.4	6.9	10.5	9.0
FeO	11.7	18.0	15.7	13.1	22.6	16.1	17.1	21.3	19.3	14.1	23.3	16.5
MnO	0.4	0.9	0.6	0.4	1.2	1.0	0.8	1.0	0.9	0.8	1.3	0.9
MgO	10.4	15.5	12.2	9.6	14.0	11.9	8.3	11.4	10.1	6.8	13.5	11.5
CaO	11.2	12.1	11.7	10.1	12.6	11.7	10.8	11.9	11.3	10.5	11.6	11.2
Na_2O	1.1	1.7	1.4	0.5	1.8	1.3	0.8	1.3	1.1	0.8	2.0	1.7
K_2O	0.4	1.6	1.0	0.4	1.0	0.7	0.4	0.9	0.6	0.4	0.8	0.6
					Atomic fraction							
Si	6.4	7.0	6.7	6.7	7.3	6.9	6.8	7.2	7.0	6.6	7.0	6.8
Ti	0.1	0.2	0.2	0.0	0.2	0.1	0.1	0.1	0.1	0.1	0.1	0.1
Al	1.3	1.9	1.6	0.9	1.7	1.4	1.0	1.5	1.3	1.3	1.9	1.6
Fe^{2+}	1.4	2.3	2.0	1.6	3.0	2.0	2.1	2.7	2.4	1.8	3.0	2.1
Mn	0.1	0.1	0.1	0.1	0.2	0.1	0.1	0.1	0.1	0.1	0.2	0.1
Mg	2.4	3.4	2.7	2.1	3.1	2.7	1.9	2.5	2.3	1.6	3.0	2.6
Ca	1.8	2.0	1.9	1.7	2.0	1.9	1.8	2.0	1.8	1.7	1.9	1.8
Na	0.3	0.5	0.4	0.2	0.5	0.4	0.2	0.4	0.3	0.2	0.6	0.5
K	0.1	0.3	0.2	0.1	0.2	0.1	0.1	0.2	0.1	0.1	0.2	0.1
H	2.0	2.0	2.0	2.0	2.0	2.0	2.0	2.0	2.0	2.0	2.0	2.0
$Mg/(Mg + Fe^{2+})$	0.5	0.7	0.6	0.4	0.7	0.6	0.4	0.5	0.5	0.3	0.6	0.6
$Fe/(Fe + Mg)$	0.3	0.5	0.4	0.3	0.6	0.4	0.5	0.6	0.5	0.4	0.7	0.5
Al IV	1.0	1.6	1.3	0.7	1.4	1.1	0.8	1.2	1.0	1.0	1.4	1.2
Na + K + Ca	2.2	2.7	2.5	2.0	2.6	2.4	2.2	2.4	2.3	2.2	2.5	2.4

In terms of atomic proportions, Si (apfu) ranges ftom 6.41–7.26, with the highest values in Kozbudaklar and Güneybudaklar. Fe^{2+} (apfu) increases from 1.97 in Kirazgedik to 2.07 in Delice, while Mg (apfu) decreases from 2.72 (Kirazgedik) to 2.56 (Delice) (Table 4). The Mg number (calculated as Mg#(Mg/[Mg + Fe^{2+}]) ranges from 0.34 to 0.70, with Kirazgedik amphiboles having the highest average (0.58), indicative of more primitive magmatic conditions. In the Mg/(Mg + Fe^{2+}) vs. Si diagram (Figure 10c), Kirazgedik amphiboles mostly plot within the magnesiohornblende field, with little representation in the tschermakite field, whereas Kozbudaklar and Delice extend from magnesiohornblende toward ferrohornblende, consistent with progressive Fe enrichment. Figure 10d reveals a systematic evolution from edenite and parasite/magnesio-hastingsite in Kirazgedik to ferro-edenite in Güneybudaklar, Kozbudaklar, and Delice, indicating increasingly oxidized, Fe-rich magmatic conditions.

Collectively, the geochemical evolution of both micas and amphiboles reflects a transition from high-temperature, Mg-rich mineral assemblages in Kirazgedik toward lower-temperature, Fe-enriched, and fluid-altered compositions in Güneybudaklar, Kozbudaklar, and Delice. These trends are coherent with whole-rock geochemistry and provide robust evidence for progressive magmatic differentiation, oxidation, and hydrothermal overprinting during the later stages of pluton emplacement.

5. Discussion

5.1. Tectono-Magmatic Framework and Temporal Constraints

Integrated geochronological, petrochemical, and mineralogical data delineate a complex, prolonged, and multi-phase magmatic evolution within the Nilüfer Mineralization

Complex (NMC) and adjacent plutonic suites, extending over a temporal window of approximately 9 million years (Figures 7–10). High-precision U–Pb zircon and Re–Os molybdenite ages constrain the timing of successive magmatic episodes, beginning with the early crystallization of the South-Tepeldağ Pluton at 54.56 ± 0.21 Ma. This is followed by granodioritic intrusions in the Gürgenyayla Pluton, dated at 51.02 ± 0.52 Ma and 51.5 ± 0.1 Ma, respectively. Importantly, molybdenite mineralization in the Güneybudaklar sector yields a Re–Os age of 49.93 ± 0.21 Ma, preceding the principal emplacement of the Topuk Pluton (48.71 ± 0.44 Ma) and its associated bodies (47.35 ± 0.21 Ma and 45.90 ± 0.29 Ma) (Table 5).

Table 5. Summary of geochronological data for the Topuk, South-Tepeldağ, and Gürgenyayla plutons, along with their associated mineralized zones. The reported ages determined using U–Pb and Re–Os dating, as specified.

Pluton	Zone Description	Rock Type	Method	Age (Ma)	Reference
South-Tepeldağ	Porphyry Cu-Mo	Monzodiorite	LA-ICP-MS U-Pb	54.56 ± 0.21	Kocatürk, et al. [14]
Gürgenyayla	Porphyry Cu-Mo	Granodiorite	SHRIMP U-Pb	51.02 ± 0.52	Altunkaynak, et al. [29]
Gürgenyayla	Porphyry Cu-Mo	Granodiorite	CA-TIMS U-Pb	51.5 ± 0.1	Rabayrol, et al. [12]
Topuk	Güneybudaklar Mineralization	Molybdenite	Re-Os	49.93 ± 0.21	This Study
Topuk	Main Body	Granodiorite	SHRIMP U-Pb	48.71 ± 0.44	Altunkaynak, et al. [29]
Topuk	Delice	Tonalite	LA-ICP-MS U-Pb	47.35 ± 0.21	Kocatürk, et al. [14]
Topuk	Delice	AF-Granite	LA-ICP-MS U-Pb	45.90 ± 0.29	Kocatürk, et al. [14]

This temporally constrained magmatic evolution corresponds to a tectonic regime governed by continued Neo-Tethyan subduction, trench retreat, and progressive slab rollback, rather than abrupt slab rollback. The absence of pervasive thermal overprinting on high-pressure/low-temperature (HP/LT) metamorphic assemblages, as documented in regional studies [24,58], supports a slab-attached configuration during crustal reworking. Thermomechanical models [59] corroborate this scenario, predicting alternating phases of trench retreat, asthenospheric upwelling, and upper crustal extension—consistent with the spatiotemporal distribution and geochemistry of NMC magmatism. More recently, Kocatürk et al. [14] proposed that the Eocene magmatic activity in the Tavşanlı Zone reflects post-subduction rollback processes evolving from an initial transpressional regime to transtensional kinematics. This geodynamic framework is consistent with the syn- to post-subduction setting of the Tavşanlı Belt, which aligns with potassic arc environments described by Müller and Groves [60], particularly post-collisional systems influenced by rollback-related mantle melting. The high-K calc-alkaline signatures and moderate Mg# observed in the NMC intrusions are similar to post-subduction intrusions in Iran and the Balkans [50,61]. Additionally, the presence of transpressive fault systems controlling magma ascent supports the model of structurally focused potassic magmatism in extensional orogenic belts [60].

Whole-rock major and trace element geochemistry reveals a coherent calc-alkaline differentiation trend across the NMC intrusions, reflecting systematic compositional evo-

lution from primitive to more evolved magmas. This geochemical continuum extends from low-silica, calc-alkaline composition in the Kirazgedik unit, through intermediate tonalitic–granodioritic phases observed in the Kozbudaklar and Delice units, and culminates in high-silica, high-K calc-alkaline granodioritic compositions in the Güneybudaklar sector (see Figure 7a–d). The majority of samples exhibit high-K calc-alkaline signatures, consistent with arc- or post-collisional magmatism. Notably, a subset of the Delice samples trends toward the shoshonitic field, suggesting more extreme potassium enrichment. This feature may reflect derivation from a metasomatically modified lithospheric mantle source, enriched in large ion lithophile elements (LILEs), or alternatively, significant crustal assimilation during magma ascent and evolution. Such geochemical signatures are commonly associated with post-orogenic tectonic environments, where lithospheric thinning and fluid fluxing facilitate the generation of potassic magmas [38,39]. The progressive depletion of compatible elements (e.g., Ni, V, Sr) and enrichment in incompatible elements (e.g., Rb, Zr, and K_2O/Na_2O) with increasing SiO_2 content strongly indicates a dominant control by fractional crystallization, particularly involving early removal of mafic (amphibole ± pyroxene) and feldspathic (plagioclase ± K-feldspar) phases. The Dy/Yb vs. SiO_2 diagram (see Figure 7e) provides additional constraints on REE partitioning during magma evolution. Kirazgedik samples, representing the earliest porphyry stage, are characterized by low SiO_2 and elevated Dy/Yb ratios, interpreted as a signature of garnet-dominated fractionation at deep crustal levels [42]. In contrast, the Kozbudaklar and Delice intrusions show intermediate Dy/Yb values and higher silica, reflecting amphibole-controlled differentiation at shallower depths. The most evolved Güneybudaklar samples display high SiO_2 and low Dy/Yb ratios, consistent with crystallization from highly fractionated, volatile-rich melts where garnet and amphibole are no longer major residual phases. Therefore, the geochemical and mineralogical trends from Kirazgedik to Güneybudaklar reflect a temporal-spatial progression from deep-seated garnet-influenced magmatism to shallow-level systems dominated by melt differentiation and volatile enrichment. This pattern is fully compatible with post-subduction slab rollback models, in which progressive decompression melting and increasing hydrous flux facilitate sustained magma ascent and crustal evolution in the Tavşanlı Belt. Moreover, REE and multi-element patterns (see Figure 9) further affirm a subduction-modified source, characterized by LREE enrichment and pronounced negative Nb, Ta, and Ti anomalies. Notably, the Güneybudaklar samples display steep REE slopes and the most pronounced negative Eu anomalies, implying advanced feldspar fractionation and residual melt evolution in the terminal phases of magmatism. Such geochemical signatures are consistent with protracted differentiation of hydrous, oxidized magmas at shallow crustal levels [62].

Biotite and amphibole chemistry across the studied units provides additional constraints on the magmatic and post-magmatic evolution, pointing to two distinct magmatic lineages. Kirazgedik samples are characterized by their calc-alkaline affinity and plot within mantle-derived, high-fO_2 fields (Figure 11a,b,d), which strongly suggest formation from hydrous, oxidized magmas originating in a subduction-influenced mantle source. The chemistry of amphiboles in these rocks further supports this interpretation, as most fall within the magmatic amphibole field and display signatures of crystallization under oxidizing conditions at relatively shallow crustal levels (Figure 11c,d). These findings are consistent with subduction-related magmatic systems where fluids released from the subducting slab enhance the oxidation state of the mantle wedge and promote amphibole stability during differentiation [63,64]. In contrast, the Güneybudaklar, Kozbudaklar, and Delice suites reveal a different evolutionary path. Their compositions trend toward more evolved, crustally influenced sources, plotting within the calc-alkaline orogenic suite with the peraluminous and anorogenic alkaline fields (Figure 11a), with Fe–Mg systematics

suggesting a mix of crustal and mantle inputs (Figure 11b). Amphiboles from these units often exhibit lower oxidation states and, in some cases, show evidence of late- or post-magmatic re-equilibration (Figure 11c,d). This implies crystallization from magmas that were less hydrous and less oxidized, likely emplaced during post-collisional tectonic phases. Together, the contrasting characteristics of these magmatic suites highlight the shift from subduction-related to post-orogenic magmatism in NMC, reflecting broader crust–mantle interaction processes over time [18,65,66].

Taken together, these petrological, geochemical, and geochronological observations support a coherent model wherein hydrous, subduction-related magmas underwent polybaric differentiation and episodic emplacement into the upper crust under conditions shaped by slab rollback and transtensional deformation. The timing of molybdenite mineralization (~49.9 Ma) coincides with the inherited zircon domains (~50–52 Ma) in the earlier phase of the Topuk Pluton, indicating that hydrothermal fluid exsolution and mineralization were temporally linked with the early felsic intrusions. This temporal coupling supports the interpretation of a vertically integrated magmatic–hydrothermal system, in which progressive fractional crystallization, moderate levels of crustal contamination, and structurally focused fluid migration played key roles in concentrating metals [1,67,68]. The transition from transpressional to transtensional tectonics likely provided extensional conduits and permeability pathways, facilitating the ascent of magmas and hydrothermal fluids during the terminal stages of arc magmatism [1,69–72].

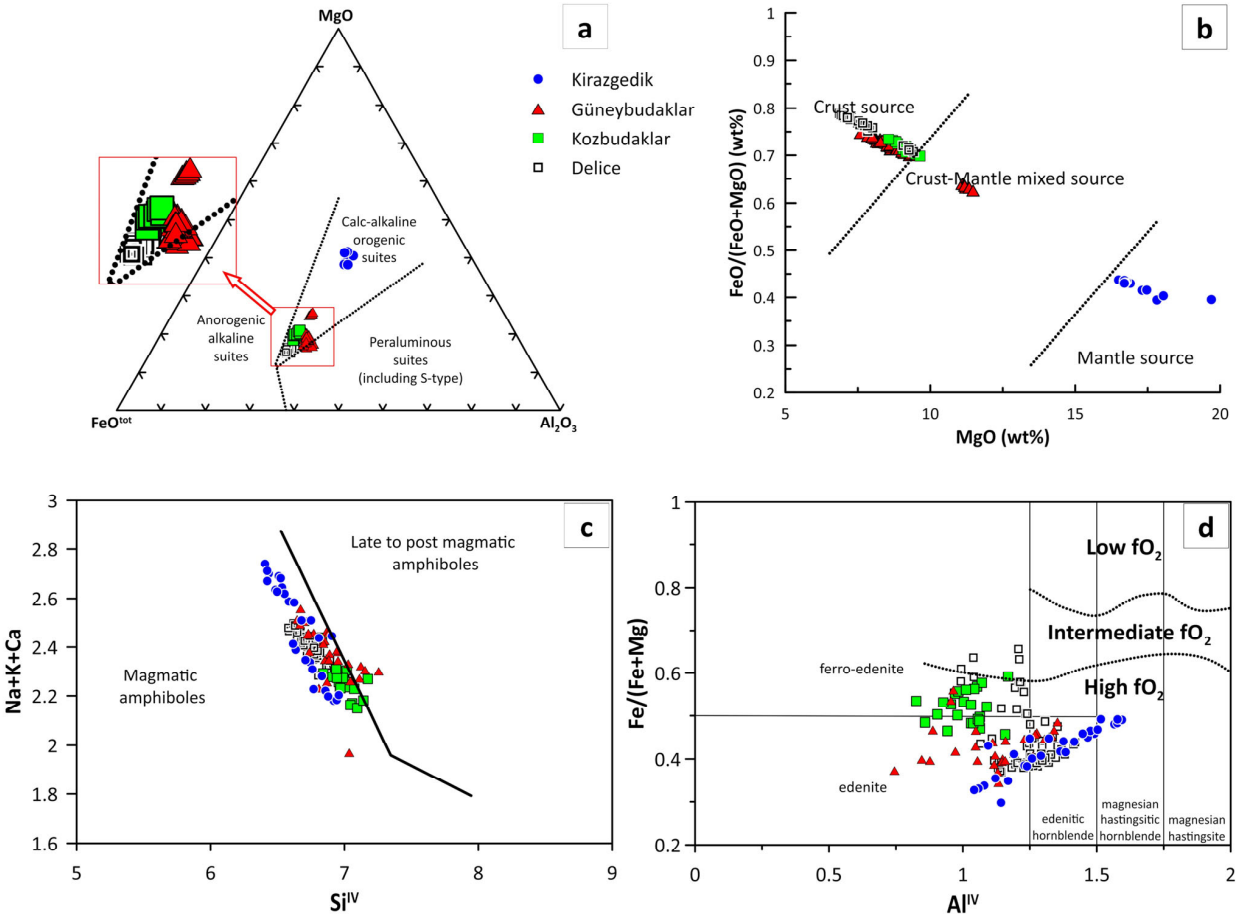

Figure 11. (**a**) MgO-FeOtot-Al_2O_3 discriminating diagrams for biotite, after Abdel-rahman [73]; (**b**) FeO/(FeO + MgO) vs. MgO (wt.%) binary diagram after Zhou [74]; (**c**) Na + K/Ca vs. Si^{IV} diagram distinguishing magmatic from late- to post-magmatic amphiboles, fields after Czamanske and Wones [75]; (**d**) Fe/(Fe + Mg) vs. Al^{IV} diagram for estimating relative oxygen fugacity, after Anderson and Smith [76].

5.2. Mineralogical Discriminants as Vectors in Exploration

Whole-rock and mineral-scale geochemistry across the NMC reveal pronounced spatial trends that integrate magmatic differentiation, volatile enrichment, and metal fertility. Among these, biotite halogen content—particularly fluorine—emerges as the most sensitive fluid-flux indicator. Fluorine concentrations in biotite decrease systematically eastward from ~1.4 wt.% at Kirazgedik to ~0.4 wt.% at Delice, whereas Cl remains uniformly low (<0.2 wt.%) (see Table 3). Notably, only biotite from the Güneybudaklar and Delice sectors simultaneously exhibits $X_{Mg} \leq 0.60$ and F ≥ 0.30 wt.%, consistent with mineralization-fertile conditions (see Table 3; Figure 10a,b). Experimental petrology demonstrates that F-rich biotite crystallizes from H_2O–F-rich melts or fluids capable of transporting high-field-strength elements (HFSEs) such as W, Mo, and Au. Low Cl/F ratios further indicate acidic, sulfur-poor fluid conditions conducive to scheelite precipitation rather than chalcopyrite [77–79].

These trends are consistent with halogen systematics observed in amphibole compositions, which offer a complementary view of magmatic–hydrothermal evolution across the belt. Halogen concentrations in amphibole and biotite reveal a coherent spatial pattern that reflects progressive volatile depletion and fluid saturation. In the Kirazgedik porphyry system, both minerals are enriched in fluorine and chlorine (F > 0.4 wt.%, Cl > 0.3 wt.%), indicating an oxidized, volatile-rich magma capable of Cu-Mo transport. By contrast, the transitional Güneybudaklar samples show persistently high Cl (>0.3 wt.%) but decreased F (to ~0.1 wt.%), suggesting late-stage degassing or fluid unmixing during skarn evolution. This is consistent with evolved potassic magmas nearing volatile saturation, as observed in global analogues [60,80]. Similar halogen patterns in the MICA1 database also differentiate fertile from barren high-K suites [60]. Although post-emplacement degassing may reduce preserved F and Cl values [81,82], the persistence of Cl-rich, F-depleted signatures in Güneybudaklar and skarn-related intrusions implies continued fluid mobility and potential for ore deposition.

A similar spatial and compositional evolution is also observed in amphibole major oxide chemistry, reinforcing the halogen-based volatile trends. Samples from the Güneybudaklar and Delice plots in the ferro-edenite and ferro-pargasite fields (see Figure 10d), showing $X_{Mg} < 0.60$ and increased Al^{IV}, and containing up to 1.0 wt.% K_2O (see Table 4)—indicative of potassic, vapor-saturated melt conditions typical of cupola-stage degassing in a skarn system [18,83]. K-rich amphiboles are commonly recognized as a characteristic feature of porphyry–skarn systems [18,84].

Whole-rock major-oxide trends reinforce this evolving volatile scenario: SiO_2 increases from about 55 wt.% in Kirazgedik quartz-monzodiorites to >75 wt.% in Delice felsic dykes, whereas Fe_2O_3 reaches ~35 wt.% in skarn samples from Kozbudaklar and Delice, coincident with peak W concentrations (>2557 ppm). This enrichment is attributed to carbonate replacement and elevated oxygen fugacity—conditions favoring W and Bi metal transport via chloride–fluoride complexes [18,78].

Highly evolved apophyses at Güneybudaklar and Delice are further characterized by Rb/Sr > 1 and Zr > 250 ppm—classic characteristics of fractionated, volatile-rich granites [49,85]. Thermometry using Ti-in-biotite and amphibole thermometry indicates temperature decrease from ~500 °C at Kirazgedik to <300 °C at Delice, while fO_2 increases—marking the shift from Cu–Mo porphyry cores to W-rich skarn halos [18,78,86].

Field relationships corroborate this mineralogical vector. Chemically evolved intrusions in Güneybudaklar and Delice are structurally controlled by faults and breccia zones that acted as conduits for late-stage fluids. Kozbudaklar represents a transitional domain—Mo rich yet W laden (>2300 ppm) with moderate F in biotite—reflecting a Mo–W skarn system retaining porphyry characteristics. Meanwhile, Kirazgedik preserves primitive

signatures (e.g., high X_{Mg} biotite, mantle-derived amphibole, Cu–Mo enrichment), typically of early compressional porphyry stages.

5.3. Thermo-Redox Evolution of Magmatic Pulses

Thermobarometric modeling based on amphibole compositions, using the empirical formulations of Ridolfi et al. [17] and magmatic fO_2 estimates from the Geo-fO_2 software (version 2.0) [87], provides critical insight into the temporal and spatial evolution of P–T–fO_2–H_2O conditions across the NMC (Supplementary Table S6). Each mineralized sector displays a distinctive and internally coherent thermodynamic trajectory, reflecting contrasting magmatic histories that align with their respective mineralization styles and geochemical signatures (Figure 12).

The Kirazgedik region is defined by amphibole compositions that cluster at high temperatures (mean ≈ 876 °C), with elevated pressures (up to 2.7 kbar), indicative of deeper magma storage (Figure 12a,b). A steep increase in ΔFMQ with decreasing temperature (up to 2.3) reflects the development of a pronounced redox gradient during rapid magma ascent, likely associated with progressive degassing and oxidation (Figure 12c). Despite these high pressures, amphibole H_2O contents remain relatively low (4.3–6.6 wt.%) (Figure 12e), suggesting that the parental magma was initially volatile-undersaturated and derived from a reduced mantle source within the sub-continental lithospheric mantle (SCLM), consistent with a compressional subduction setting [14,78]. The observed thermal–redox evolution—characterized by increasing oxidation with ascent—is compatible with the destabilization of early magnetite shells around the porphyry core and the influx of oxidized, slab-derived fluids [78,88].

In contrast, the Güneybudaklar region displays moderately lower crystallization temperatures (mean ≈ 826 °C) and a narrower pressure range (0.7–2.0 kbar) (Figure 12a,b), consistent with shallower magma emplacement. The ΔFMQ values in this region are relatively stable, with a median of approximately 1.4, suggesting that redox conditions were established early and remained constant throughout cooling (Figure 12c). Amphibole H_2O contents in this region are higher on average (4.7–7.3 wt.%) (Figure 12e), indicating a melt that was more hydrous and more oxidized than its Kirazgedik region. Although most amphiboles in Güneybudaklar display this oxidized and stable signature, a subset exhibits Kirazgedik-like trends in the ΔFMQ–H_2O relationship (Figure 12d), pointing to the possibility of early slab-fluid influx followed by overprinting by crustally buffered, oxidized fluids during later stages of skarn development [13,77,89]. This hybrid signature underscores the transitional nature of Güneybudaklar, straddling the boundary between porphyry-type magmatism and the onset of skarn-forming processes.

The Kozbudaklar region records the lowest average crystallization temperatures (mean ≈ 780 °C) and pressures (0.9–1.7 kbar) across the complex (Figure 12a,b). Its ΔFMQ–T trend is nearly flat (Figure 12c), centered around a ΔFMQ of ~1.1, reflecting little to no change in oxidation state during cooling. Amphibole H_2O contents are consistently high (6.2–7.4 wt.%) (Figure 12e), indicating that the magmatic system was water-rich and likely fluid-saturated through its evolution. The thermal and redox characteristics of Kozbudaklar suggest a shallow emplacement regime and limited magmatic recharge, consistent with the development of static, iron-rich skarn systems rather than dynamic porphyry-type roots.

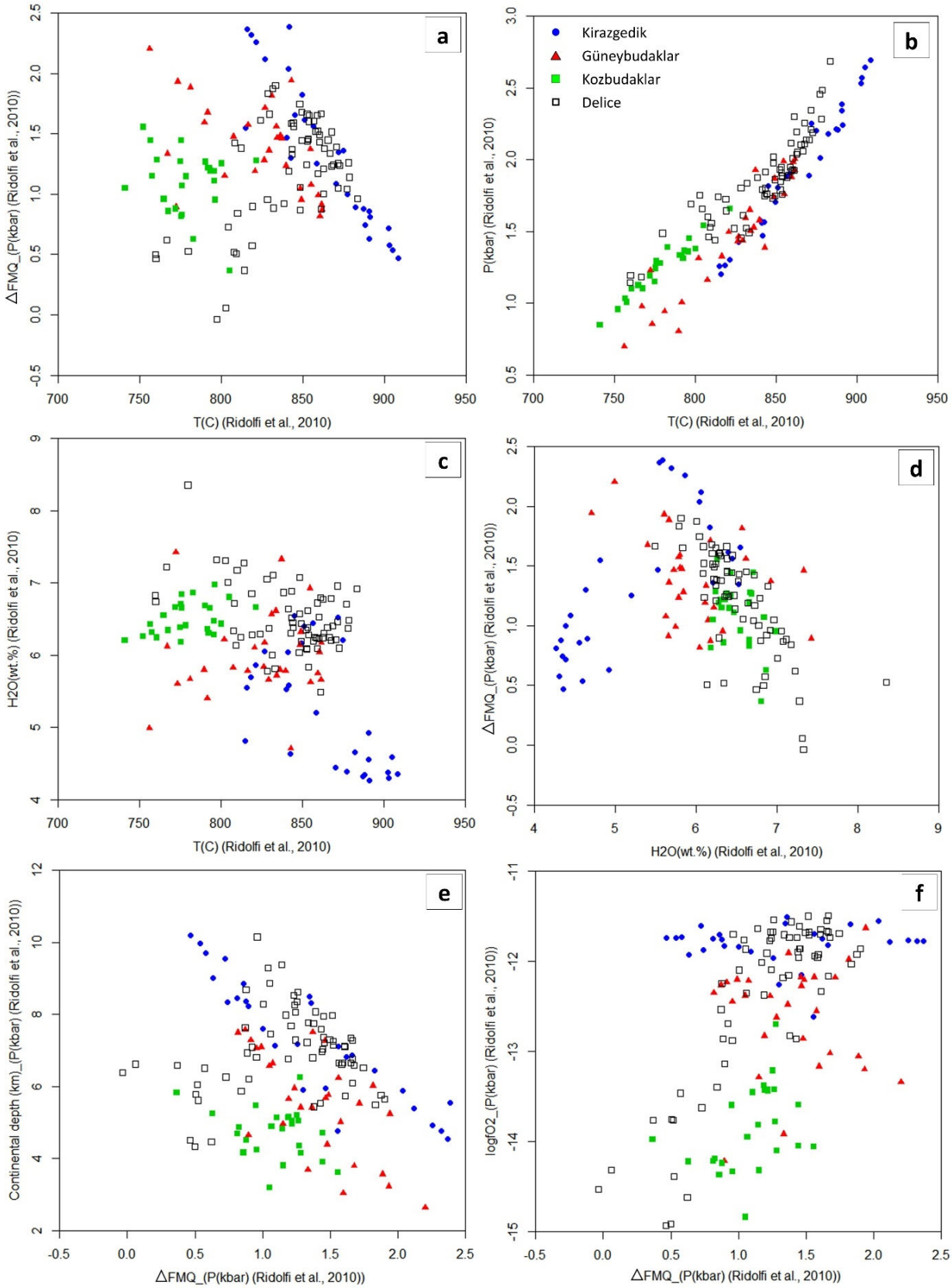

Figure 12. Thermobarometric and redox parameter estimations for amphiboles from the Kirazgedik, Güneybudaklar, Kozbudaklar, and Delice sectors [17,87]: (**a**) ΔFMQ (kbar) vs. temperature (°C); (**b**) Pressure (kbar) vs. temperature (°C); (**c**) H_2O content (wt.%) vs. temperature (°C); (**d**) ΔFMQ (kbar) vs. H_2O content (wt.%); (**e**) Continental crustal depth (km) vs. ΔFMQ (kbar); (**f**) $\log_{10}fO_2$ (kbar) vs. ΔFMQ (kbar).

The Delice region exhibits crystallization temperatures and pressures similar to those of Güneybudaklar (Figure 12a,b), but it is distinguished by a more complex and variable redox evolution. Amphibole ΔFMQ values at Delice range from 0.1 to 2.7, with an irregular decline as temperature decreases (Figure 12c). This oscillatory ΔFMQ behavior may reflect episodic magma recharge, heterogeneous wall–rock interactions, or differences in degassing efficiency during magmatic crystallization. Pressure estimates for Delice are broad (1.1–2.7 kbar), suggesting that intrusions were emplaced at multiple crustal levels (Figure 12b). Despite these fluctuations in fO_2, amphibole H_2O contents remain consistently high (up to 8.3 wt.%) (Figure 12e), indicating that the magmas were volatile-saturated systems and retain high fluid flux potential—ideal for the formation of W–Ce–Fe skarn assemblages [85,90].

A crucial distinction among sectors is observed in the relationship between ΔFMQ and calculated H_2O contents (Figure 12d). In Kirazgedik, a positive correlation between fO_2 and H_2O implies that the system became increasingly oxidized as juvenile, slab-derived fluids were fluxed. This trajectory is characteristic of early-stage magmas influenced by oxidizing volatiles such as SO_2 and Cl-bearing components released during slab dehydration [13,91,92]. These fluids are known to enhance both redox state and metal transport capacity in arc settings [77,93]. In contrast, the Güneybudaklar, Kozbudaklar, and Delice sectors exhibit either inverse or scattered ΔFMQ–H_2O relationships, suggesting decoupling of oxidation and volatile content. This pattern is interpreted as evidence of significant interaction with shallow-level or external fluids, including meteoric or metamorphic waters, which dilute primary magmatic signals and impose localized redox buffering through wall–rock reaction [85,94]. The divergence from the oxidized juvenile fluid signature of Kirazgedik highlights a fundamental shift in fluid provenance and redox control during the transition from compressional subduction to slab rollback.

The distribution of ΔFMQ values across sectors delineates a systematic redox structure within the magmatic plumbing system of the NMC (Figure 12f). Most samples cluster between ΔFMQ 1 and 1.5, consistent with moderately oxidized arc magmas [78,91]. However, amphiboles from Kirazgedik and parts of Güneybudaklar extend to higher ΔFMQ values, reflecting the influence of deeply sourced, oxidized slab-derived fluids. In contrast, the Kozbudaklar and Delice sectors, which crystallized at similar pressures, exhibit ΔFMQ values closer to the arc average, suggesting a progressive redox homogenization of the magmatic system over time. This convergence likely reflects long-term equilibration through magma recharge–mixing cycles, prolonged residence in upper crustal chambers, and overprinting by crustally derived or meteoric fluids [85,95]. Collectively, these trends support a vertically integrated, evolving magmatic–hydrothermal system that matured through both internal differentiation and external fluid interaction during the late stages of arc evolution in a rollback-dominated tectonic setting [13,92].

5.4. Litho-Structural Controls and Metallogenic Model

The coexistence of porphyry Cu-Mo and skarn W deposits is geologically uncommon due to their contrasting magmatic and redox requirements. Porphyry Cu-Mo systems are typically derived from oxidized, hydrous, calc-alkaline magmas, often associated with magnetite-series granitoids in convergent margin settings [1,96]. These magmas are characterized by high oxygen fugacity (fO_2), which facilitates the transport and deposition of chalcophile metals like Cu and Mo as sulfide complexes [97]. In contrast, W-bearing skarn systems generally form in association with reduced, ilmenite-series granitoids, often of S-type affinity, where lower fO_2 favors the stability of tungstate species (e.g., scheelite), and the involvement of crustal-derived magmas is more pronounced [7,98]. Nevertheless, spatial and temporal associations of both deposit types have been reported in several

metallogenic provinces, challenging conventional redox-based models: the Yechangping Mo-porphyry/W-skarn system (East Qinling, China) and the giant Zhuxi W-Cu deposit (South China). These mining districts worldwide illustrate instances where porphyry copper-molybdenum (Cu-Mo) systems are spatially and temporally associated with tungsten (W) skarn mineralization. Although this coexistence is relatively rare, it underscores the role of specific geologic conditions—such as evolving magmatic oxidation states and mixed magmatic sources—in facilitating the simultaneous evolution of these mineralization styles.

In the Yechangping porphyry-skarn system (East Qinling, Luanchuan District, China), the Luanchuan metallogenic district hosts giant Mo deposits that grade into W-bearing skarns. For instance, the Yechangping deposit is a representative porphyry-skarn Mo-W system, featuring porphyry-style molybdenum mineralization accompanied by a tungsten-bearing skarn zone [99]. Other nearby intrusions (e.g., Nannihu–Sandaozhuang) similarly contain porphyry Mo orebodies with adjacent W-rich skarns [100]. These systems formed from Jurassic granitoids of intermediate oxidation state, and they illustrate how a single magmatic-hydrothermal system can generate Mo-sulfide ore in the cupola (porphyry) and scheelite in peripheral skarns [99]. Geological studies of Luanchuan deposits indicate that magma differentiation and fluid phase evolution led to varying fO_2 conditions—high fO_2 fluids precipitated Mo sulfides in the porphyry core, whereas relatively lower fO_2 at the limestone contacts favored scheelite deposition in skarns [99]. This explains the co-occurrence of Cu/Mo and W mineralization in what was once thought to be an exclusively "oxidized" porphyry environment. While in South China's Jiangnan ore belt (northern Nanling region), most granitoids are reduced ilmenite-series, typically yielding W–Sn skarns. However, recent discoveries in the Late Jurassic–Early Cretaceous Jiangnan belt include several giant W deposits with unusual Cu or Mo enrichment [101]. The Dahutang W–Cu deposit in Jiangxi is a prime example—it contains an estimated 1.1 million tonnes of WO_3 along with significant copper byproducts [101]. Such W–Cu skarn systems are interpreted to result from hybrid magmas or evolving redox conditions: an initially reduced granite generated the bulk of the tungsten (scheelite) mineralization, but pockets of more oxidized, sulfur-rich melt or magma mingling introduced chalcopyrite (Cu) mineralization in tandem [101,102]. In other cases, like the Yangchuling W–Mo deposit (Jiangnan belt), zircons record mixed Ce^{4+}/Ce^{3+} ratios, suggesting the magma fO_2 fluctuated during crystallization [102]. These Chinese examples show that W-skarn formation is not strictly limited to purely reduced systems—if a pluton's oxygen fugacity increases slightly (or a minor oxidized magma invades), it can carry chalcophile metals like Cu/Mo without fully suppressing scheelite deposition.

In our study, the NMC represents a vertically superimposed, laterally zoned magmatic–hydrothermal system developed during the late stages of subduction-related arc magmatism and post-subduction extension. The mineralization architecture observed—progressing from early Cu–Mo fractured porphyries to distal, relatively reduced W-dominant skarns—is controlled by a synergistic interplay between magma evolution, redox and volatile state, emplacement depth, and the inherited upper crustal structure. The temporal progression from Kirazgedik (~54.6 Ma) to Delice (~45.9 Ma) reflects an evolving magmatic system transitioning from mafic, mantle-derived, reduced melts to felsic, volatile-saturated, and oxidized intrusions. Early-stage Kirazgedik intrusions are interpreted as high-pressure, oxidant-deficient melts derived from a metasomatized sub-continental lithospheric mantle (SCLM), characterized by low H_2O and moderate fO_2, as inferred from amphibole-based thermobarometry and low Cl/F ratios in biotite [14,78] (Figure 13). The Cu-Mo-Au-W association observed in both the Kirazgedik and Güneybudaklar systems closely resembles other porphyry-style deposits such as Skouries and Cadia Ridge-way,

which are hosted in oxidized, high-K magmas [60,103]. Geochemical indicators—such as elevated fO_2 (~+1.5 ΔFMQ) and Cl-enriched amphiboles—collectively point to a fertile, volatile-saturated magmatic source. These features align well with the genetic models of porphyry ore formation proposed by Richards [8] and broadly applied in exploration frameworks [60].

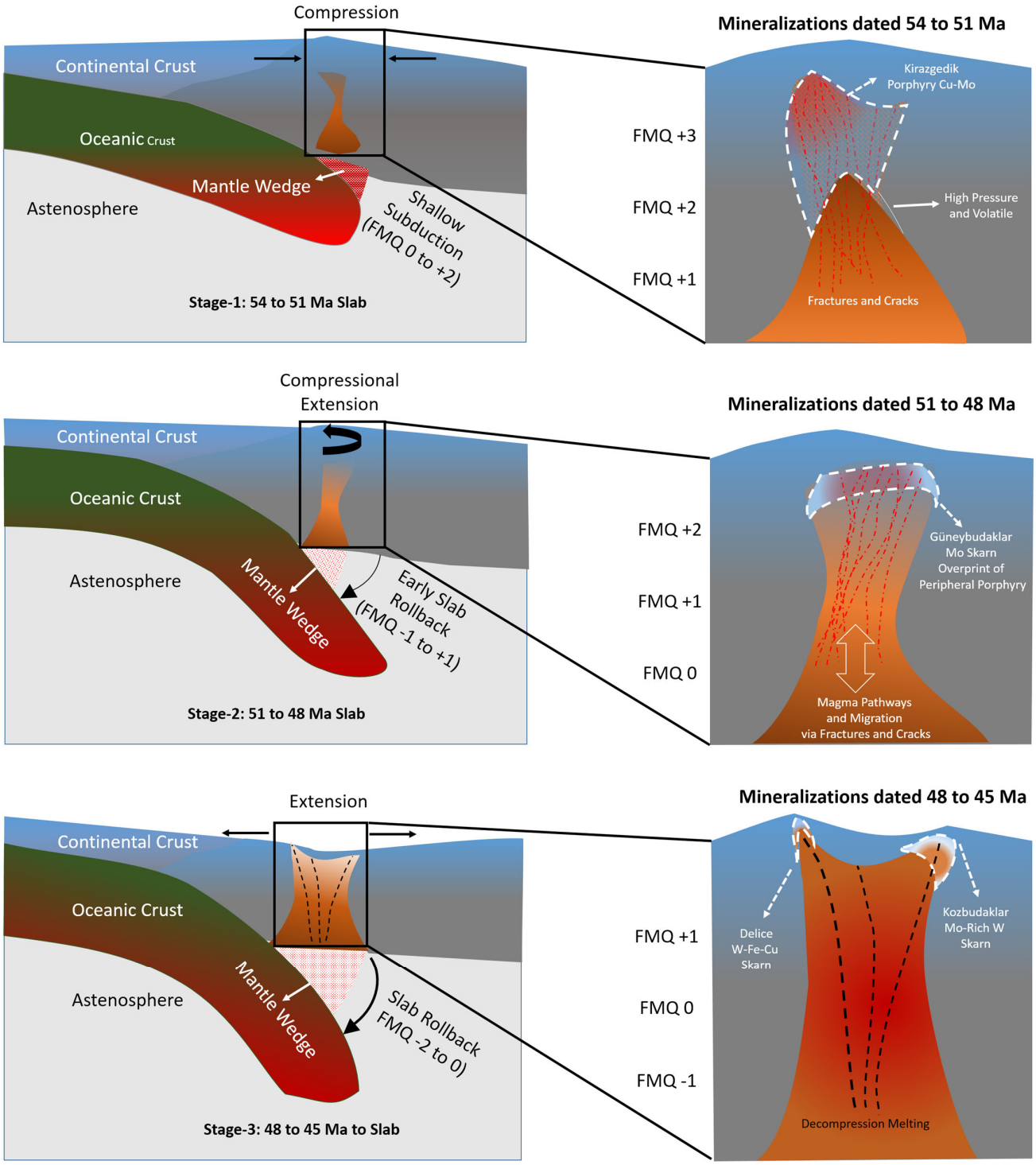

Figure 13. Tectonomagmatic evolution and associated mineralization stages in the NMC region from 54 to 45 Ma, illustrating slab dynamics, redox conditions (FMQ), and ore-forming processes.

As the system evolved, fractional crystallization, crustal assimilation, and the ingress of slab-derived oxidized fluids promoted higher H_2O content and elevated fO_2 condi-

tions. These processes facilitated the formation of W, Mo, and Bi-rich mineralizing fluids, particularly in Güneybudaklar and Kozbudaklar. The elevated Al^{IV} and K_2O contents in amphiboles from these sectors, combined with high SiO_2 and Rb/Sr ratios in host rocks, indicate that these magmas had undergone extensive differentiation and Cl saturation at shallower crustal levels (~0.7–2.0 kbar), forming the cupola zones of evolving porphyry–skarn transitions [18,89]. Delice, the youngest and most evolved center, preserves felsic, fluid-charged intrusions with the highest H_2O contents and lowest crystallization temperatures (~<300 °C), suggestive of late-stage, low-pressure skarn-forming conditions. Amphibole ΔFMQ values at Delice fluctuate widely, possibly due to episodic magma pulses or interaction with external fluids (e.g., meteoric or metamorphic), reflecting an unstable redox environment during crystallization and late-stage hydrothermal fluid flow.

In addition to early-stage porphyry mineralization associated with oxidized high-K calc-alkaline magmas, the progressive rollback of the subducting slab likely triggered mantle wedge widening and enhanced contributions from carbonate platform melting (Figure 13). This evolution introduced reducing agents into the mantle wedge and facilitated variable redox states across the NMC intrusions. Similarly, the increased crustal input into high-K magmas—typical of post-collisional arc settings—is genetically linked to Cu-Mo-W-Au porphyry–skarn transitions [104,105].

Metal precipitation exhibited depth dependency; in deeper levels, magnetite and sulfide saturation promoted Cu and Mo deposition. Conversely, in shallower, acidic, and sulfur-poor conditions (e.g., Delice), scheelite and associated tungstate phases were stabilized by oxidized, F-bearing fluids [77,78]. Structural controls played a key role in channeling magmas and hydrothermal fluids. Major mineralized centers such as Güneybudaklar and Delice are aligned with oblique-slip fault zones and breccia corridors, interpreted as conduits formed during slab rollback-driven transtensional deformation [24,58]. These tectonic features enabled vertical superposition of porphyry, skarn, and epithermal mineralization styles, preserved as a continuous spectrum from deep-seated porphyry roots to shallow-level skarn caps and vein systems [106,107]. The absence of significant thermal overprinting on the surrounding HP–LT metamorphic basement is consistent with slab-attached rollback scenarios, wherein fluid and heat transport remained spatially restricted along structurally reactivated zones [85,91].

Integrating mineral chemistry, thermobarometry, redox proxies, and structural data, the NMC exemplifies a complete porphyry–skarn system evolving within a post-subduction tectonic context. Its metallogenic sequence—ranging from Cu–Mo (Kirazgedik) to Mo–W–Bi–Au (Güneybudaklar/Kozbudaklar), and finally W–Fe–Ce (Delice)—reflects both spatial zonation and temporal magmatic evolution from mantle-derived to crust-dominated sources. This progression parallels analogous systems in the Andes and the Central Asian Orogenic Belt [85,108], where oxidized, hydrous magmas and structurally complex settings control metal enrichment. The NMC thus serves as a representative hybrid porphyry–skarn system, shaped by concurrent changes in tectonics, magma chemistry, and lithospheric architecture.

6. Conclusions

The mineralized systems of the westernmost Eocene Tavşanlı Metallogenic Belt, exemplified by the Nilüfer Mineralization Complex (NMC) in NW Türkiye, record a systematic and spatially coherent evolution from high-temperature, oxidized porphyry-style Cu-Mo systems to more reduced, volatile-depleted W-Mo-bearing skarns. This metallogenic progression reflects a broader magmatic differentiation trend coupled with evolving emplacement depths and redox states during the post-subduction tectonic regime.

Kirazgedik represents the earliest and most thermodynamically distinct mineralization phase, formed from deep-seated, oxidized, hydrous magmas crystallizing at elevated temperatures (~930 °C) and pressures (~2.7 kbar). This porphyry Cu-Mo system is interpreted as the product of early post-subduction arc magmatism, marked by high magmatic fO_2 and water content. The transitional Güneybudaklar system, constrained by Re–Os molybdenite ages (~49.9 Ma), developed under moderately oxidized (ΔFMQ ~ 1.8–0.5) and water-rich conditions, facilitating Mo and W enrichment at the porphyry–skarn interface. Kozbudaklar, in contrast, reflects a more evolved and degassed magmatic state, where reduced conditions favored scheelite (W) mineralization in a distal skarn environment. Delice captures the most complex fluid history, characterized by felsic intrusions into carbonate rocks and recording a wide redox-volatility spectrum. The coexistence of both oxidized and reduced fluid signatures suggests prolonged, multi-stage fluid evolution involving both magmatic and externally derived components, as well as intense fluid–rock interaction during retrograde alteration. Collectively, these systems illustrate a continuous, genetically linked porphyry–skarn evolution controlled by progressive magmatic differentiation, redox evolution, and crustal emplacement depth, all modulated by a regional tectonic shift from transpression to transtension during slab rollback. Amphibole and mica compositions provide robust proxies for reconstructing magmatic conditions (P–T–fO_2–H_2O) and are shown to be effective tools for assessing magmatic fertility and fluid evolution in complex post-subduction systems. Integrated petrological, mineralogical, and geochemical analyses delineate the mineralization potential and refine exploration models in porphyry–skarn terranes of the Western Tethyan domain.

Supplementary Materials: The following supporting information can be downloaded at: https://www.mdpi.com/article/10.3390/min15080792/s1. Table S1. Sample Metadata; Table S2. Whole Rock All; Table S3. Ore All; Table S4. Mica EPMA; Table S5. Amphibole EPMA; Table S6. Amphibole Calculations; Figure S1. Representative BSE images of amphiboles and micas from Kirazgedik samples; Figure S2. Representative BSE images of amphiboles and micas from Güneybudaklar samples; Figure S3. Representative BSE images of amphiboles and micas from Kozbudaklar samples; Figure S4. Representative BSE images of amphiboles and micas from Delice samples.

Author Contributions: Conceptualization, H.K., M.K. (Mustafa Kumral), R.A.C. and A.A.; methodology, H.K., M.K. (Mustafa Kaya) and A.A.; software, H.K. and M.K. (Mustafa Kaya); validation, H.K., H.S., R.A.C. and A.A.; formal analysis, H.K., M.K. (Mustafa Kaya) and R.A.C.; investigation, H.K., M.K. (Mustafa Kumral), H.S., M.K. (Mustafa Kaya), R.A.C. and A.A.; data curation, H.K., M.K. (Mustafa Kumral), H.S., M.K. (Mustafa Kaya), R.A.C. and A.A.; writing—original draft preparation, H.K., M.K. (Mustafa Kaya) and A.A.; writing—review and editing, H.K., M.K. (Mustafa Kumral), R.A.C. and A.A.; visualization, H.K., M.K. (Mustafa Kumral), H.S., R.A.C. and A.A.; supervision, M.K. (Mustafa Kumral). All authors have read and agreed to the published version of the manuscript.

Funding: This research was funded by the Scientific and Technological Research Council of Türkiye (TÜBİTAK) through graduate student research grants awarded to Hüseyin Kocatürk and is derived from the corresponding author's PhD dissertation, completed at Istanbul Technical University (ITU, Turkey). Additionally, it was funded by the Scientific Research Project (BAP Project No: MHD-2025-46403) of Istanbul Technical University (ITU, Turkey).

Data Availability Statement: The data are available Tables 1–5.

Acknowledgments: Hüseyin Kocatürk gratefully acknowledges the financial support received from the Scientific and Technological Research Council of Türkiye (TÜBİTAK) through graduate student research grants, which contributed to the advancement of his doctoral studies and the production of this article as part of his PhD dissertation at Istanbul Technical University. The authors also acknowledge additional funding provided by Istanbul Technical University (ITU, Turkey) under the Scientific Research Project (BAP Project No: MHD-2025-46403). They express their gratitude to the

Geochemistry Research Laboratories (JAL) group of ITU for their valuable support in conducting analytical research, as well as to Beril Tanç Kaya. Additionally, the authors are much more grateful to the anonymous Editor and three reviewers for their constructive comments and helpful suggestions, which greatly improved the manuscript.

Conflicts of Interest: The authors declare no conflicts of interest.

References

1. Sillitoe, R.H. Porphyry copper systems. *Econ. Geol.* **2010**, *105*, 3–41. [CrossRef]
2. Cooke, D.R.; Hollings, P.; Walshe, J.L. Giant porphyry deposits: Characteristics, distribution, and tectonic controls. *Econ. Geol.* **2005**, *100*, 801–818. [CrossRef]
3. Kaya, M.; Kumral, M.; Yalçın, C.; Abdelnasser, A. Genesis and Evolution of the Yolindi Cu-Fe Skarn Deposit in the Biga Peninsula (NW Turkey): Insights from Genetic Relationships with Calc-Alkaline Magmatic Activity. *Minerals* **2023**, *13*, 1304. [CrossRef]
4. Kaya, M.; Kumral, M.; Yalçın, C.; Abdelnasser, A. Sulfur and Carbon–Oxygen Isotopic Geochemistry and Fluid Inclusion Characteristics of the Yolindi Cu-Fe Skarn Mineralization, Biga Peninsula, NW Turkey: Implications for the Source and Evolution of Hydrothermal Fluids. *Minerals* **2023**, *13*, 1542. [CrossRef]
5. Karaman, M.; Kumral, M.; Yildirim, D.K.; Doner, Z.; Afzal, P.; Abdelnasser, A. Delineation of the porphyry-skarn mineralized zones (NW Turkey) using concentration–volume fractal model. *Geochemistry* **2021**, *4*, 125802. [CrossRef]
6. Abdelnasser, A.; Kumral, M.; Zoheir, B.; Yilmaz, H. Evolution of the Tepeoba porphyry-skarn Cu-Mo-Au deposit, NW Turkey: New mineralogical and geochemical findings. *Ore Geol. Rev.* **2022**, *147*, 104967. [CrossRef]
7. Meinert, L.D.; Dipple, G.M.; Nicolescu, S.; Hedenquist, J.W.; Thompson, J.F.H.; Goldfarb, R.J.; Richards, J.P. World Skarn Deposits. In *Economic Geology 100th Anniversary Volume*; Society of Economic Geologists: Littleton, CO, USA, 2005; pp. 299–336.
8. Richards, J. Metallogeny of the Neo-Tethys arc in central Iran. In *Mineral Exploration and Sustainable Development*; Millpress: Rotterdam, The Netherlands, 2003; pp. 1237–1239.
9. Kocatürk, H. Genesis and Tectono-Metallogenic Evolution of Gold-Tungsten-Copper-Molybdenum (Au-W-Cu-Mo) Mineralizations Associated with Eocene Granitoids Around Uludağ (Bursa). Ph.D. Thesis, Istanbul Technical University, Istanbul, Turkiye, 2024.
10. McFall, K.; Roberts, S.; McDonald, I.; Boyce, A.J.; Naden, J.; Teagle, D. Rhenium enrichment in the Muratdere Cu-Mo (Au-Re) porphyry deposit, Turkey: Evidence from stable isotope analyses (δ34S, δ18O, δD) and laser ablation-inductively coupled plasma-mass spectrometry analysis of sulfides. *Econ. Geol.* **2019**, *114*, 1443–1466. [CrossRef]
11. Kuşcu, İ.; Tosdal, R.; Gençalioğlu-Kuşcu, G. Episodic Porphyry Cu (-Mo-Au) formation and associated magmatic evolution in Turkish Tethyan collage. *Ore Geol. Rev.* **2019**, *107*, 119–154. [CrossRef]
12. Rabayrol, F.; Hart, C.J.; Friedman, R.M.; Spikings, R.A. Diachronous Magmatic and Cu-Au-Mo Metallogenic Responses to Slab Roll-Back Initiation from Northwest Anatolia to the Balkans, Western Tethyan Eocene Magmatic Belt. In *Tectonomagmatic Influences on Metallogeny and Hydrothermal Ore Deposits: A Tribute to Jeremy P. Richards*; Sholeh, A., Wang, R., Eds.; Society of Economic Geologists, Inc.: Littleton, CO, USA, 2021; Volume 1, pp. 17–28.
13. Orhan, A. Evolution of the Mo-rich scheelite skarn mineralization at Kozbudaklar, Western Anatolia, Turkey: Evidence from mineral chemistry and fluid inclusions. *Ore Geol. Rev.* **2017**, *80*, 141–165. [CrossRef]
14. Kocatürk, H.; Kumral, M.; Creaser, R.A.; DuFrane, S.A.; Ünlüer, A.T.; Sendir, H.; Döner, Z.; Kaya, M.; Özdamar, Ş.; Abdelnasser, A. Magma nature and tectono-magmatic context of the Eocene Uludağ granitoids (NW-Türkiye): Insights into the Cenozoic geodynamics of the Tethyan Orogenic Belt. *Geochemistry* **2024**, *84*, 126170. [CrossRef]
15. Okay, A.I.; Tüysüz, O. Tethyan sutures of northern Turkey. *Geol. Soc. Lond. Spec. Publ.* **1999**, *156*, 475–515. [CrossRef]
16. Kuşcu, İ.; Tosdal, R.M.; Gençalioğlu-Kuşcu, G. Porphyry-Cu Deposits of Turkey. In *Mineral Resources of Turkey*; Springer: Berlin/Heidelberg, Germany, 2019; pp. 337–425.
17. Ridolfi, F.; Renzulli, A.; Puerini, M. Stability and chemical equilibrium of amphibole in calc-alkaline magmas: An overview, new thermobarometric formulations and application to subduction-related volcanoes. *Contrib. Mineral. Petrol.* **2010**, *160*, 45–66. [CrossRef]
18. Ridolfi, F.; Renzulli, A. Calcic amphiboles in calc-alkaline and alkaline magmas: Thermobarometric and chemometric empirical equations valid up to 1,130 °C and 2.2 GPa. *Contrib. Mineral. Petrol.* **2012**, *163*, 877–895. [CrossRef]
19. Li, X.; Zhang, C.; Almeev, R.R.; Zhang, X.-C.; Zhao, X.-F.; Wang, L.-X.; Koepke, J.; Holtz, F. Electron probe microanalysis of Fe2+/ΣFe ratios in calcic and sodic-calcic amphibole and biotite using the flank method. *Chem. Geol.* **2019**, *509*, 152–162. [CrossRef]
20. Shafaii Moghadam, H.; Xiao, W.; Karsli, O.; Aydin, F.; He, Y.; Chiaradia, M.; Griffin, W.L. Copper endowment of the magmatic rocks from Eastern Sakarya Zone (Türkiye): Insights from zircon and apatite geochemical evolution. *Contrib. Mineral. Petrol.* **2025**, *180*, 38. [CrossRef]

21. Duan, X.-X.; Ju, Y.-F.; Chen, B.; Wang, Z.-Q. Garnet geochemistry of reduced Skarn system: Implications for fluid evolution and Skarn formation of the Zhuxiling W (Mo) deposit, China. *Minerals* **2020**, *10*, 1024. [CrossRef]
22. Carter, L.C.; Tapster, S.R.; Williamson, B.J.; Buret, Y.; Selby, D.; Rollinson, G.K.; Millar, I.; Parvaz, D.B. A rapid change in magma plumbing taps porphyry copper deposit-forming magmas. *Sci. Rep.* **2022**, *12*, 17272. [CrossRef]
23. Plunder, A.; Agard, P.; Chopin, C.; Okay, A.I. Geodynamics of the Tavşanlı zone, western Turkey: Insights into subduction/obduction processes. *Tectonophysics* **2013**, *608*, 884–903. [CrossRef]
24. Okay, A.I.; Harris, N.B.; Kelley, S.P. Exhumation of blueschists along a Tethyan suture in northwest Turkey. *Tectonophysics* **1998**, *285*, 275–299. [CrossRef]
25. Plunder, A.; Agard, P.; Chopin, C.; Pourteau, A.; Okay, A.I. Accretion, underplating and exhumation along a subduction interface: From subduction initiation to continental subduction (Tavşanlı zone, W. Turkey). *Lithos* **2015**, *226*, 233–254. [CrossRef]
26. Okay, A.I. Tavşanli zone: The northern subducted margin of the Anatolide-Tauride block. *Bull. Miner. Res. Explor.* **2011**, *142*, 191–221.
27. Okay, A.I.; Satir, M. Geochronology of Eocene plutonism and metamorphism in northwest. *Geodin. Acta* **2006**, *19*, 251–266. [CrossRef]
28. Sarifakioğlu, E.; Özen, H.; Winchester, J.A. Whole rock and mineral chemistry of ultramafic-mafic cumulates from the Orhaneli (Bursa) ophiolite, NW Anatolia. *Turk. J. Earth Sci.* **2009**, *18*, 55–83. [CrossRef]
29. Altunkaynak, Ş.; Sunal, G.; Aldanmaz, E.; Genç, C.Ş.; Dilek, Y.; Furnes, H.; Foland, K.A.; Yang, J.; Yıldız, M. Eocene Granitic Magmatism in NW Anatolia (Turkey) revisited: New implications from comparative zircon SHRIMP U–Pb and 40Ar–39Ar geochronology and isotope geochemistry on magma genesis and emplacement. *Lithos* **2012**, *155*, 289–309. [CrossRef]
30. Selby, D.; Creaser, R.A. Macroscale NTIMS and microscale LA-MC-ICP-MS Re-Os isotopic analysis of molybdenite: Testing spatial restrictions for reliable Re-Os age determinations, and implications for the decoupling of Re and Os within molybdenite. *Geochim. Cosmochim. Acta* **2004**, *68*, 3897–3908. [CrossRef]
31. Markey, R.; Stein, H.J.; Hannah, J.L.; Zimmerman, A.; Selby, D.; Creaser, R.A. Standardizing Re–Os geochronology: A new molybdenite reference material (Henderson, USA) and the stoichiometry of Os salts. *Chem. Geol.* **2007**, *244*, 74–87. [CrossRef]
32. Smoliar, M.I.; Walker, R.J.; Morgan, J.W. Re-Os ages of group IIA, IIIA, IVA, and IVB iron meteorites. *Science* **1996**, *271*, 1099–1102. [CrossRef]
33. Orhan, A.; Demirbilek, M.; Mutlu, H. Mineral and whole-rock geochemistry of the Topuk Granitoid (Bursa, Western Anatolia, Turkey). In Proceedings of the EGU General Assembly Conference Abstracts, Vienna, Austria, 27 April–2 May 2014; p. 5103.
34. Orhan, A.; Mutlu, H. Geochemical characteristics and rare-earth element distributions of Kozbudaklar W-Skarn Deposit (Bursa, Western Anatolia). *Bull. Miner. Res. Explor.* **2017**, *155*, 115–130. [CrossRef]
35. Kumral, M.; Abdelnasser, A.; Budakoglu, M. Geochemistry of Hydrothermal Alteration Associated with Cenozoic Intrusion-Hosted Cu-Pb-Zn Mineralization at Tavşanlı Area, Kütahya, NW Turkey. *Minerals* **2016**, *6*, 13. [CrossRef]
36. Doner, Z.; Unluer, A.T.; Özdamar, Ş.; Sarıkaya, O.; Roden, M.F.; Kaya, M.; Kocaturk, H.; Kumral, M.; Esenli, F. The origin of alkali granites and Th-U ± REE enrichments in Kestanbol Magmatic complex (NW Anatolia) revisited: Evidences from bulk-rock geochemistry and isotopic data, zircon UPb, biotite Ar/Ar and apatite (UTh)/He geochronology. *Lithos* **2024**, *484–485*, 107751. [CrossRef]
37. Janoušek, V.; Farrow, C.M.; Erban, V. Interpretation of whole-rock geochemical data in igneous geochemistry: Introducing Geochemical Data Toolkit (GCDkit). *J. Petrol.* **2006**, *47*, 1255–1259. [CrossRef]
38. El Bouseily, A.; El Sokkary, A. The relation between Rb, Ba and Sr in granitic rocks. *Chem. Geol.* **1975**, *16*, 207–219. [CrossRef]
39. Foley, S.F.; Venturelli, G.; Green, D.H.; Toscani, L. The ultrapotassic rocks: Characteristics, classification, and constraints for petrogenetic models. *Earth-Sci. Rev.* **1987**, *24*, 81–134. [CrossRef]
40. Rollinson, H. *Using Geochemical Data: Evolution, Presentation, Interpretation*; Longman Scientific and Technical: London, UK, 1993; p. 352.
41. Le Maitre, R.W. *Igneous Rocks: A Classification and Glossary of Terms*; Cambridge University Press: Cambridge, UK, 2002; p. 237.
42. Davidson, J.; Turner, S.; Handley, H.; Macpherson, C.; Dosseto, A. Amphibole "sponge" in arc crust? *Geology* **2007**, *35*, 787–790. [CrossRef]
43. McKenzie, D.; O'nions, R. Partial Melt Distributions from Inversion of Rare Earth Element Concentrations. *J. Petrol.* **1991**, *32*, 1021–1091. [CrossRef]
44. Pearce, J.A.; Harris, N.B.; Tindle, A.G. Trace element discrimination diagrams for the tectonic interpretation of granitic rocks. *J. Petrol.* **1984**, *25*, 956–983. [CrossRef]
45. Bonin, B. Do coeval mafic and felsic magmas in post-collisional to within-plate regimes necessarily imply two contrasting, mantle and crustal, sources? A review. *Lithos* **2004**, *78*, 1–24. [CrossRef]
46. Debon, F.; Le Fort, P. A chemical–mineralogical classification of common plutonic rocks and associations. *Earth Environ. Sci. Trans. R. Soc. Edinb.* **1983**, *73*, 135–149. [CrossRef]
47. Miyashiro, A. Volcanic rock series in island arcs and active continental margins. *Am. J. Sci.* **1974**, *274*, 321–355. [CrossRef]

48. Peccerillo, A.; Taylor, S. Geochemistry of Eocene calc-alkaline volcanic rocks from the Kastamonu area, northern Turkey. *Contrib. Mineral. Petrol.* **1976**, *58*, 63–81. [CrossRef]
49. Laurent, A.; Janousek, V.; Magna, T.; Schulmann, K.; Mikova, J. Petrogenesis and geochronology of a post-orogenic calc-alkaline magmatic association: The Zulova Pluton, Bohemian Massif. *J. Geosci.* **2014**, *59*, 415–440. [CrossRef]
50. Pearce, J. Sources and settings of granitic rocks. *Epis. J. Int. Geosci.* **1996**, *19*, 120–125. [CrossRef]
51. Gill, J.B. *Orogenic Andesites and Plate Tectonics*; Springer Science & Business Media: Berlin/Heidelberg, Germany, 1981; Volume 16, p. 390.
52. Pearce, J.A. Trace element characteristics of lavas from destructive plate boundaries. In *Orogenic Andesites and Related Rocks*; Wiley: Hoboken, NJ, USA, 1982; pp. 528–548.
53. Boynton, W.V. Geochemistry of Rare Earth Elements: Meteorite Studies. In *Rare Earth Element Geochemistry*; Henderson, P., Ed.; Elsevier: New York, NY, USA, 1984; pp. 63–114. [CrossRef]
54. Sun, S.-S.; McDonough, W. Chemical and isotopic systematics of oceanic basalts: Implications for mantle composition and processes. *Geol. Soc. Lond. Spec. Publ.* **1989**, *42*, 313–345. [CrossRef]
55. Tischendorf, G.; Gottesmann, B.; Förster, H.-J.; Trumbull, R.B. On Li-bearing micas: Estimating Li from electron microprobe analyses and an improved diagram for graphical representation. *Mineral. Mag.* **1997**, *61*, 809–834. [CrossRef]
56. Nachit, H.; Ibhi, A.; Ohoud, M.B. Discrimination between primary magmatic biotites, reequilibrated biotites and neoformed biotites. *Comptes Rendus Géosci.* **2005**, *337*, 1415–1420. [CrossRef]
57. Leake, B.E.; Woolley, A.R.; Arps, C.E.; Birch, W.D.; Gilbert, M.C.; Grice, J.D.; Hawthorne, F.C.; Kato, A.; Kisch, H.J.; Krivovichev, V.G. Nomenclature of amphiboles; report of the subcommittee on amphiboles of the International Mineralogical Association, Commission on New Minerals and Mineral Names. *Can. Mineral.* **1997**, *35*, 219–246.
58. Pourteau, A.; Oberhänsli, R.; Candan, O.; Barrier, E.; Vrielynck, B. Neotethyan closure history of western Anatolia: A geodynamic discussion. *Int. J. Earth Sci.* **2016**, *105*, 203–224. [CrossRef]
59. Tirel, C.; Brun, J.-P.; Burov, E.; Wortel, M.; Lebedev, S. A plate tectonics oddity: Caterpillar-walk exhumation of subducted continental crust. *Geology* **2013**, *41*, 555–558. [CrossRef]
60. Müller, D.; Groves, D.I. *Potassic Igneous Rocks and Associated Gold-Copper Mineralization*, 4th ed.; Springer: Cham, Switzerland, 2016.
61. Müller, D.; Rock, N.; Groves, D. Geochemical Discrimination between Shoshonitic and Potassic Volcanic Rocks in Different Tectonic Settings: A Pilot Study. *Mineral. Petrol.* **1992**, *46*, 259–289. [CrossRef]
62. Park, J.-W.; Campbell, I.H.; Chiaradia, M.; Hao, H.; Lee, C.-T. Crustal magmatic controls on the formation of porphyry copper deposits. *Nat. Rev. Earth Environ.* **2021**, *2*, 542–557. [CrossRef]
63. Putirka, K. Special Collection: Rates and Depths of Magma Ascent on Earth: Amphibole thermometers and barometers for igneous systems and some implications for eruption mechanisms of felsic magmas at arc volcanoes. *Am. Mineral.* **2016**, *101*, 841–858. [CrossRef]
64. Luo, C.-H.; Wang, R.; Nebel, O.; Li, Q.-W. Amphibole fractionation as a key driver for oxidation of magmas in convergent margins. *Earth Planet. Sci. Lett.* **2024**, *641*, 118851. [CrossRef]
65. Frost, B.R.; Barnes, C.G.; Collins, W.J.; Arculus, R.J.; Ellis, D.J.; Frost, C.D. A geochemical classification for granitic rocks. *J. Petrol.* **2001**, *42*, 2033–2048. [CrossRef]
66. Moyen, J.-F. High Sr/Y and La/Yb ratios: The meaning of the "adakitic signature". *Lithos* **2009**, *112*, 556–574. [CrossRef]
67. Heinrich, C.A.; Candela, P.A. Fluids and ore formation in the Earth's crust. In *Treatise on Geochemistry*, 2nd ed.; Elsevier: Amsterdam, The Netherlands, 2014; Volume 13, pp. 1–28.
68. Codeço, M.S.; Weis, P.; Andersen, C. Numerical modeling of structurally controlled ore formation in magmatic-hydrothermal systems. *Geochem. Geophys. Geosystems* **2022**, *23*, e2021GC010302. [CrossRef]
69. Blanquat, M.D.S.; Tikoff, B.; Teyssier, C.; Vigneresse, J.L. Transpressional kinematics and magmatic arcs. *Geol. Soc. Lond. Spec. Publ.* **1998**, *135*, 327–340. [CrossRef]
70. Murphy, J.B. Igneous rock associations 7. Arc magmatism I: Relationship between subduction and magma genesis. *Geosci. Can.* **2006**, *33*, 145–168.
71. Oriolo, S.; Gómez, A.L.R.; Maffini, M.N.; Oyhantçabal, P.; Demarco, M.M.; Vargas Perucca, M.S.; Bastías Torres, M.V.; Rubinstein, N.A. Transtension, brittle-ductile shear zones and hydrothermal ore deposits: Towards quantitative structural and kinematic models. *J. Struct. Geol.* **2024**, *185*, 105173. [CrossRef]
72. Contreras-Reyes, E.; Díaz, D.; Bello-González, J.P.; Slezak, K.; Potin, B.; Comte, D.; Maksymowicz, A.; Ruiz, J.A.; Osses, A.; Ruiz, S. Subduction zone fluids and arc magmas conducted by lithospheric deformed regions beneath the central Andes. *Sci. Rep.* **2021**, *11*, 23078. [CrossRef]
73. Abdel-rahman, A.-F.M. Nature of Biotites from Alkaline, Calc-alkaline, and Peraluminous Magmas. *J. Petrol.* **1994**, *35*, 525–541. [CrossRef]
74. Zhou, Z. The origin of intrusive mass in Fengshandong, Hubei province. *Acta Petrol. Sin.* **1986**, *2*, 59–70.

75. Czamanske, G.K.; Wones, D.R. Oxidation during magmatic differentiation, Finnmarka complex, Oslo area, Norway: Part 2, the mafic silicates1. *J. Petrol.* **1973**, *14*, 349–380. [CrossRef]
76. Anderson, J.L.; Smith, D.R. The effects of temperature and fO2 on the Al-in-hornblende barometer. *Am. Mineral.* **1995**, *80*, 549–559. [CrossRef]
77. Audétat, A.; Günther, D.; Heinrich, C.A. Causes for large-scale metal zonation around mineralized plutons: Fluid inclusion LA-ICP-MS evidence from the Mole Granite, Australia. *Econ. Geol.* **2000**, *95*, 1563–1581. [CrossRef]
78. Loucks, R.R. Distinctive composition of copper-ore-forming arcmagmas. *Aust. J. Earth Sci.* **2014**, *61*, 5–16. [CrossRef]
79. Icenhower, J.P.; London, D. Partitioning of fluorine and chlorine between biotite and granitic melt: Experimental calibration at 200 MPa H_2O. *Contrib. Mineral. Petrol.* **1997**, *127*, 17–29. [CrossRef]
80. Reed, M.H.; Palandri, J. Sulfide mineral precipitation from hydrothermal fluids. *Rev. Mineral. Geochem.* **2006**, *61*, 609–631. [CrossRef]
81. Chelle-Michou, C.; Rottier, B.; Caricchi, L.; Simpson, G. Tempo of magma degassing and the genesis of porphyry copper deposits. *Sci. Rep.* **2017**, *7*, 40566. [CrossRef] [PubMed]
82. Chelle-Michou, C.; Chiaradia, M. Amphibole and apatite insights into the evolution and mass balance of Cl and S in magmas associated with porphyry copper deposits. *Contrib. Mineral. Petrol.* **2017**, *172*, 105. [CrossRef]
83. Cai, W.-y.; Wang, K.-y.; Li, J.; Fu, L.-j.; Li, S.-d.; Yang, H.; Konare, Y. Genesis of the Bagenheigeqier Pb–Zn skarn deposit in Inner Mongolia, NE China: Constraints from fluid inclusions, isotope systematics and geochronology. *Geol. Mag.* **2021**, *158*, 271–294. [CrossRef]
84. Zhao, X.; Yang, Z.; Zheng, Y.; Liu, Y.; Tian, S.; Fu, Q. Geology and genesis of the post-collisional porphyry–skarn deposit at Bangpu, Tibet. *Ore Geol. Rev.* **2015**, *70*, 486–509. [CrossRef]
85. Chiaradia, M. Adakite-like magmas from fractional crystallization and melting-assimilation of mafic lower crust (Eocene Macuchi arc, Western Cordillera, Ecuador). *Chem. Geol.* **2009**, *265*, 468–487. [CrossRef]
86. Song, G.; Cook, N.J.; Li, G.; Qin, K.; Ciobanu, C.L.; Yang, Y.; Xu, Y. Scheelite geochemistry in porphyry-skarn W-Mo systems: A case study from the Gaojiabang Deposit, East China. *Ore Geol. Rev.* **2019**, *113*, 103084. [CrossRef]
87. Li, W.; Cheng, Y.; Yang, Z. Geo-fO2: Integrated software for analysis of magmatic oxygen fugacity. *Geochem. Geophys. Geosyst.* **2019**, *20*, 2542–2555. [CrossRef]
88. Wilkinson, J.J. Triggers for the formation of porphyry ore deposits in magmatic arcs. *Nat. Geosci.* **2013**, *6*, 917–925. [CrossRef]
89. Dilles, J.; Barton, M.; Johnson, D.; Proffett, J.; Einaudi, M. *Part I. Contrasting Styles of Intrusion-Associated Hydrothermal Systems*; Guidebook Series; Society of Economic Geologists, Inc.: Littleton, CO, USA, 2000; Volume 32, pp. 1–162.
90. Krawczynski, M.J.; Grove, T.L.; Behrens, H. Amphibole stability in primitive arc magmas: Effects of temperature, H_2O content, and oxygen fugacity. *Contrib. Mineral. Petrol.* **2012**, *164*, 317–339. [CrossRef]
91. Richards, J.P. Magmatic to hydrothermal metal fluxes in convergent and collided margins. *Ore Geol. Rev.* **2011**, *40*, 1–26. [CrossRef]
92. Keppler, H. Fluids and trace element transport in subduction zones. *Am. Mineral.* **2017**, *102*, 5–20. [CrossRef]
93. Candela, P.A.; Piccoli, P.M. Magmatic processes in the development of porphyry-type ore systems. In *One Hundredth Anniversary Volume*; Hedenquist, J.W., Thompson, J.F.H., Goldfarb, R.J., Richards, J.P., Eds.; Society of Economic Geologists: Washington, DC, USA, 2005.
94. Heinrich, C.A. Fluid-fluid interactions in magmatic-hydrothermal ore formation. *Rev. Mineral. Geochem.* **2007**, *65*, 363–387. [CrossRef]
95. Dilles, J.H.; Kent, A.J.R.; Wooden, J.L.; Tosdal, R.M.; Koleszar, A.; Lee, R.G.; Farmer, L.P. Zircon compositional evidence for sulfur-degassing from ore-forming arc magmas*. *Econ. Geol.* **2015**, *110*, 241–251. [CrossRef]
96. Ishihara, S. The granitoid series and mineralization. In *Seventy-Fifth Anniversary Volume: 1905–1980*; Skinner, B.J., Ed.; Economic Geology Publishing Company: McLean, VA, USA, 1981.
97. Ballard, J.R.; Palin, J.M.; Campbell, I.H. Relative oxidation states of magmas inferred from Ce(IV)/Ce(III) in zircon: Application to porphyry copper deposits of northern Chile. *Contrib. Mineral. Petrol.* **2002**, *144*, 347–364. [CrossRef]
98. Candela, P.; Piccoli, P. Model ore-metal partitioning from melts into vapor and vapor/brine mixtures. In *Magma, Fluids and Ore Deposits*; Thompson, J., Ed.; Mineralogical Association of Canada Short Course: Québec, QC, Canada, 1995; Volume 23, pp. 101–127.
99. Huang, P.-C.; Yu, J.; Yao, J.-M.; Qi, N.; Qiu, Z.-W.; Chen, Y.-J. Case study of the large-scale Mo-W mineralization in Eastern Qinling, China: Geology and genesis of the Yechangping porphyry-skarn system. *Ore Geol. Rev.* **2024**, *165*, 105867. [CrossRef]
100. Zhan, Q.; Gao, X.-Y.; Meng, L.; Zhao, T.-P. Ore genesis and fluid evolution of the Sandaozhuang supergiant W-Mo skarn deposit, southern margin of the North China Craton: Insights from scheelite, garnet and clinopyroxene geochemistry. *Ore Geol. Rev.* **2021**, *139*, 104551. [CrossRef]
101. Ouyang, Y.; Hou, Z.; He, X.; Pan, X.; Wei, J.; Zeng, R.; Chen, Q. Geochronological, geochemical and isotopic constraints on the genesis of Cu mineralization in the giant Zhuxi W–Cu deposit, South China. *Ore Geol. Rev.* **2025**, *184*, 106767. [CrossRef]

102. Wu, S.; Sun, W.; Wang, X. A new model for porphyry W mineralization in a world-class tungsten metallogenic belt. *Ore Geol. Rev.* **2019**, *107*, 501–512. [CrossRef]
103. Sillitoe, R. Characteristics and controls of the largest porphyry copper-gold and epithermal gold deposits in the circum-Pacific region. *Aust. J. Earth Sci.* **1997**, *44*, 373–388. [CrossRef]
104. Soloviev, S.G.; Kryazhev, S.G.; Shapovalenko, V.N.; Dvurechenskaya, S.S.; Semenova, D.V.; Kalinin, Y.A.; Voskresensky, K.I.; Sidorova, N.V. The Glafirinskoe and related skarn Cu-Au-W-Mo deposits in the Northern Altai, SW Siberia, Russia: Geology, igneous geochemistry, zircon U-Pb geochronology, mineralization, and fluid inclusion characteristics. *Ore Geol. Rev.* **2021**, *138*, 104382. [CrossRef]
105. Soloviev, S.G. Late Palaeozoic high-K calc-alkaline to shoshonitic series magmatism and related W (–Mo–Cu–Au) metallogeny of the Kyrgyz Tien Shan, Central Asia. *Geol. Soc. Lond. Spec. Publ.* **2024**, *551*, 231–258. [CrossRef]
106. Kumral, M.; Kabiru, M.; Aydogan, M.S.; Kocaturk, H.; Unluer, A.T. The Soma polymetallic hydrothermal Pb–Zn-Cu($\pm$ Mo $\pm$ Ag $\pm$ Au) mineralizations in the south of Biga Peninsula, NW Turkey: Constraints from mineralogy, geochemistry, and fluid inclusion data. *Arab. J. Geosci.* **2022**, *15*, 1172. [CrossRef]
107. Kocaturk, H.; Sendir, H.; Kumral, M.; Unluer, A.; Budakoglu, M. Isotopic Features and Fluid Charecterization of Ore Forming Process Gurgenyayla and Bogazova Plutons (Kütahya/Bursa/Bilecik-Turkey). *Magmat. Earth Relat. Strateg. Met. Depos.* **2018**, 138–141.
108. Mao, J.; Pirajno, F.; Cook, N. Mesozoic metallogeny in East China and corresponding geodynamic settings—An introduction to the special issue. *Ore Geol. Rev.* **2011**, *43*, 1–7. [CrossRef]